Porosity and permeability evolution in the Tuaheni Landslide Complex at Hikurangi margin from IODP Sites U1517 and U1519

Jade Dutilleul, Sylvain Bourlange, Yves Géraud, Thierry Reuschlé

Porosity and permeability evolution in the Tuaheni Landslide Complex at Hikurangi margin from IODP Sites U1517 and U1519

Jade Dutilleul[a]*, S. Bourlange[b], Y. Géraud[b] and T. Reuschlé[c]

[a]*University of Lorraine, CNRS, GeoRessources, F–54000 Nancy, France, now at Earthquake Research Institute, The University of Tokyo, Tokyo, Japan*

[b]*University of Lorraine, CNRS, GeoRessources, F–54000 Nancy, France*

[c] *Université de Strasbourg, CNRS, Institut Terre et Environnement de Strasbourg, UMR 7063, 5 rue Descartes, Strasbourg F-67084, France*

*jade.dutilleul@univ–lorraine.fr; jdutilleul@eri.u-tokyo.ac.jp

Several mechanisms involving excess pore pressure related to gas hydrate have been proposed to explain active creeping at landslides such as the north Hikurangi margin Tuaheni Landslide Complex (TLC). Cores and logging data were retrieved by the International Ocean Discovery Program (IODP) Expeditions 372 and 375 from the South TLC at Site U1517. Here, the evolutions of porosity, pore structure and permeability are determined to assess the compaction state in the landslide and compare it with that of the undeformed sequence at Site U1519. Although no evidence of gas hydrate in the landslide at Site U1517 was identified by the cruise, zones suspected to host gas hydrates below the landslide or at Site U1519 are characterised by higher porosity, pore diameter and permeability. We show that most of the sedimentary section is in hydrostatic conditions, except the base of the TLC at Site U1517 and a zone below the base of the gas hydrate stability zone at Site U1519. These zones might be candidates for excess pore pressure build-up. There is no obvious evidence of the involvement of gas hydrate in active creeping at the TLC, which is more likely induced by hydrogeomechanical processes.

Keywords: porosity, permeability, pore pressure, gas hydrates, MICP, NMR, CEC, landslide, Hikurangi, IODP

Introduction

The Tuaheni Landslide Complex (TLC) is situated on the upper slope of the relatively sediment-starved north Hikurangi margin (Mountjoy et al., 2009), where the Pacific Plate obliquely subducts, at a ~5.0 cm/y rate, beneath the Australian Plate (Wallace et al., 2004) (Figure 1a). In the study area, the Pacific Plate is composed of the Cretaceous-aged volcanic Hikurangi Plateau protruded by seamounts and blanketed by a ~1.0–1.5 kilometres-thick Cenozoic to Mesozoic sedimentary cover. The TLC is composed of Quaternary shelf-edge clinoform sequences (Pedley et al., 2010), with wedge-shaped thinning-upwards siliciclastic sediments (Barnes et al., 1991; Alexander et al., 2010), above Cenozoïc and Late Mesozoïc sediments (Field et al., 1997; Barnes et al., 2002; Mountjoy and Barnes, 2011). Based on morphological differences, Mountjoy et al. (2009) divided the TLC into a north (North TLC) and a south component (South TLC) (Figure 1b), both feeding the Tuaheni Basin with Quaternary sediments (Mountjoy et al., 2009; 2014). The South TLC also contributes to filling the Paritu Basin with debris. Arcuate internal scarps characterise the North TLC. The South TLC, on which this study is focused, is constituted by irregular rough landslide debris downslope of large scars. The South TLC is thought to be divided into two mass-transport deposit (MTD) units (Mountjoy et al., 2014; Böttner et al., 2018; Gross et al., 2018; Kuhlmann et al., 2019). These units are separated by an intra-debris negative-polarity seismic reflector, interpreted as a décollement layer that may localise excess pore pressure (Gross et al., 2018).

Based on bathymetry data, Mountjoy et al. (2009) suggested that the South TLC initially formed as a catastrophic failure and is now actively creeping, rather than growing through repeated failures leading to downslope transport of new source material, as commonly admitted for submarine landslides (Mulder and Cochonat, 1996;

Canals et al., 2004). However, the mechanisms triggering this active slow deformation remain unclear. First, Mountjoy et al. (2009) related creeping with high pore pressure induced by gas expulsion, sediment loading or earthquakes. Such creeping would conduct to small-scale compressional and extensional features across the landslide, which have not been observed. On the contrary, the South TLC is marked by a transition from a compressive upper sediment-supplied mass to an extensive part near the toe where sediments are removed (Figure 2a) (Mountjoy et al., 2014; Barnes et al., 2019a). Later, Mountjoy et al. (2013, 2014) observed that the upper limit of creeping occurs downslope of where a hydrate-related bottom-simulating-reflector (BSR) (and thus the base of gas hydrate stability (BGHS)) cutting through the landslide reaches the seafloor. This zone also corresponds to the transition between compressional and extensional deformation of the South TLC. They suggested that gas hydrates may be involved in ongoing slow deformation and proposed three possible mechanisms: 1) gas hydrate dissociation at the BGHS; 2) a hydrate pressure valve model implying the repeated hydrofracturing and weakening of the gas hydrate zone with a transfer of the overpressure accumulated underneath low-permeability gas hydrate-bearing sediments to the landslide mass where the BGHS approaches the seafloor and 3) a hydrate glacier model with gas hydrate-bearing sediments showing creeping behaviour (Mountjoy et al., 2013, 2014; Barnes et al., 2019a).

The International Ocean Discovery Program (IODP) Expedition 372 drilled, logged and cored Site U1517 in the extensional zone of the south component (Figures 1b and 2) to investigate the mechanisms behind creeping in the TLC and their possible links with gas hydrate occurrence. Gas hydrates were identified beneath the landslide based on drilling results, discarding the hydrate glacier model hypothesis (Barnes et al., 2019c; Screaton et al., 2019). Two other sites were initially planned to be drilled in the

compressive part of the landslide and a reference site outside the landslide mass (Pecher et al., 2014). Even if this second drilling phase was not achieved (Barnes et al., 2019a), the outcomes from Site U1517 (Barnes et al., 2019b) can be interpreted in light of the properties of the sedimentary section at Site U1519 (Barnes et al., 2019a). Site U1519 was drilled, logged and partially cored ~15 kilometres at the northeast of Site U1517, in the western part of the Tuaheni basin fed by the north component of the TLC (Figures 1b and 3) (Barnes et al., 2019c). Gas hydrate occurrence is inferred from direct observations at Site U1519 (Barnes et al., 2019c).

Here, we document the evolution of compaction state from porosity and permeability from measurements on core samples and logging-while-drilling (LWD) data at Site U1517 through the extensional part of the South TLC and beneath, and at Site U1519. Compaction state may be interpreted in terms of pore pressure development. Elevated pore pressure is commonly associated with a local anomalously high porosity compared to a reference porosity-effective stress curve (Conin et al., 2011) determined assuming hydrostatic fluid pressure and uniaxial compaction conditions (Screaton et al., 2002). However, the porosity routinely measured on core samples during IODP expeditions cannot be directly used for compaction state analysis because it is based on the total water content of samples. Total water content includes interstitial water, which is contained in pores, and water bound in hydrous minerals such as smectite (Brown and Ransom, 1996; Henry, 1997). Smectite-bound water is mainly released in the pore space by dehydration to illite, which is generally assumed to occur in a temperature range of 60–150°C (Freed and Peacor, 1989; Kastner et al., 2014). In contrast, interstitial water is expelled from the pore structure by pore collapse induced by compaction as sediments are buried (Moore and Vrolijk, 1992). Thus, interstitial water is truly representative of the compaction state (Henry, 1997; Henry and

Bourlange, 2004; Conin et al., 2011). Hence, we quantify interstitial porosity by correcting total porosity measured on samples from the smectite-bound water content to determine the compaction state at both sites. We also compare permeability deduced from pore size distribution with the permeability measured on two samples (cores 17H6 and 29F3 at 97.43 and 157.83 mbsf respectively) in a triaxial cell under effective hydrostatic confining pressure approaching in-situ stress conditions. Finally, we discuss the porosity and permeability dataset in terms of pore pressure development at both Sites U1517 and U1519. We address the hypotheses (i.e. gas hydrates are involved in creeping in the TLC either through gas hydrate dissociation at the BGHS or hydrate pressure valve effect) and antitheses (i.e. creeping is induced by other mechanisms such as repeated small-scale seafloor failure or liquefaction of coarse silt beds) suggested during IODP Expedition 372 (see Barnes et al., 2019a for details) as possible mechanisms triggering slow deformation in the TLC.

Material and data

Site U1517

Site U1517 provided core samples and in-situ geophysical data including LWD data, and temperature and pressure measurements down to ~205 mbsf (Figure 4a). Five lithological, seismic and logging units were identified onboard (Barnes et al., 2019b). Lithological Unit I (~0–3 mbsf) corresponds to Holocene–aged greenish-grey silty clay. Units II, III and IV are Late Pleistocene-aged. Unit II (~3–41 mbsf) is composed of a succession of stacked turbidites with alternating layers of mud (i.e. clayey silt to silty clay) and greenish-grey sand beds. Unit III (~41–67 mbsf) corresponds to matrix–supported MTDs with thin to medium bedded convoluted mud layers and alternating layers of greenish-grey silt and clay. Unit IV (~67–103 mbsf) is a greenish-grey to dark

greenish grey massive clayey silty hemipelagic sequence with MTDs at the top and punctuated with silty turbidites at the base. Unit V (~103–187 mbsf) is a Middle Pleistocene mixed slope sequence including clayey to clayey–silt hemipelagites, sandy turbidites, MTDs and ash layers near the bottom of the hole.

Above the upper part of the preslide interval (~67-203 mbsf), the South TLC mass was interpreted to be composed of Unit II (upper debris unit) and Unit III (lower debris unit) (Mountjoy et al., 2014; Gross et al., 2018; Barnes et al., 2019b; Luo et al., 2020), with the décollement for creeping ~37 mbsf corresponding to the intra-debris negative polarity reflector of Gross et al. (2018). Mountjoy et al. (2014) suggested that the upper and lower units were genetically linked. This model has been recently challenged by studies that highlight different source and/or emplacement mechanisms. Luo et al. (2020) suggest that the landslide was formed by two different depositional events corresponding to Units II and III, while Couvin et al. (2020) propose that the landslide is only composed of the upper Unit II.

The base of the gas hydrate stability zone (BGHS) has been interpreted to occur ~162 mbsf prior to drilling (Gross et al., 2018; Barnes et al., 2019b; Screaton et al., 2019, 2020) or between ~85 and 128 mbsf (Sultan, 2020). Indication for gas hydrate occurrence was only found in Unit V (Figure 4) (Barnes et al., 2019b; Screaton et al., 2019, 2020; Sultan, 2020).

Site U1519

Site U1519 was drilled and logged down to 650 mbsf across three seismic units: 1) horizontally layered basin–fill including stacked MTDs and turbiditic sequences (~0–281 mbsf), the upper MTD being associated with the North TLC (Mountjoy et al., 2009, 2014; Barnes et al., 2019c), 2) southeast–dipping layered slope sequences of MTDs truncated at the unconformity between seismic Units 1 and 2 (~281–546 mbsf) and the

top (~546–650 mbsf) of a northwest-dipping and eroded hanging-wall of an inactive northwest-dipping splay fault that lies ~500 metres beneath the bottom of Site U1519 (Figure 3). Site U1519 crosscuts a weak reflector at ~560 mbsf interpreted as a possible BSR. Several intervals were cored: ~0–23 mbsf at hole D, ~0–86 mbsf at hole E and ~10–164 mbsf, ~250–288 mbsf and ~518–640 mbsf at hole C. Based on core examination, two lithological units were identified during the cruise (Barnes et al., 2019c) (Figure 5). Unit I corresponds to Holocene to late middle Pleistocene dark greenish grey mud to mudstone (i.e. silty clay(stone) to clayey silt(stone)) associated with hemipelagic settling with an ash layer occurring few meters below the seafloor. Unit I is correlated with seismic Unit 1 and logging Unit 1. Seismic and logging Units 2 and 3 correspond to lithologic Unit II, including middle to early Pleistocene light greenish-grey mudstone with scattered interbeds of silt and very fine sand, medium to coarse sand, and contorted mudstone interpreted as MTDs. Gas hydrate-bearing sediments were sampled in the lower part of the hole in core 25R4 (~627 mbsf, Figure 5) (Barnes et al., 2019c).

Methods

This study is based on 1) onboard data including LWD data and measurements on core samples and 2) post-cruise analysis of 24 and 40 core samples retrieved at Site U1517 and U1519, respectively. Samples were selected near the samples that were used for pore water composition analysis onboard. Samples were conditioned for shipping and stored at chilled temperature (2–8°C) in vacuum–sealed plastic bags with a sponge saturated with seawater to retain moisture.

175 ***Porosity***

176 *Total connected porosity*

177 We calculated the total connected porosity (ϕ_t) with a Micromeritics® AccuPyc
178 II 1340 helium-displacement pycnometer using the procedure after Blum (1997) that
179 was also followed onboard (Wallace et al., 2019; Pecher et al., 2019).

180 *Bound water content*

181 Clay bound water includes 1) water molecules absorbed in the interlayer space
182 that are usually organised into layers and 2) water molecules adsorbed on smectite
183 external surfaces and are electrostatically bounded to hydrated cations compensating the
184 negative charge of smectite layers. Clay-bound water content (ϕ_b) was calculated using
185 Equation (1):

186 $$\phi_b = n\frac{M_w}{\rho_w} CEC\, \rho_g \left(1-\phi_t\right) \qquad (1)$$

187 based on the cation exchange capacity (CEC, in mol/kg) that is a proxy for hydrous to
188 non-hydrous minerals content ratio, the water molar mass (M_w = 0.018kg/mol) and
189 density ¿ = 1024 kg/m^3), the grain density ($\rho_g$in kg/m^3) and n the average number of
190 water molecules per cation charge related to the number of water layers in the clay
191 interlayer space. The average number of water molecules per cation charge is typically
192 determined from the relationship between the CEC and the volume of chloride-free
193 water per volume of grains (Figure 6) that is derived from the soluble chloride content
194 of the sample (Henry and Bourlange, 2004; Conin et al., 2011; Daigle et al., 2015a;
195 Dutilleul et al., 2020a; 2020b). The average number of water molecules per cation
196 charge commonly ranges 6–8, 12–16, and 18–24 for one, two or three water layers
197 respectively (Henry, 1997). All the samples at Sites U1517 and U1519 show low CEC
198 values <0.2 mol/kg and thus do not show a specific bound water ratio versus CEC trend

from which n can be inferred (see Henry and Bourlange, 2004; Dutilleul et al., 2020a for further details). We used the average value of n=15 which is typical of smectite with two water layers occurring in marine sediments (Kastner et al., 2014), following the results of Dutilleul et al. (2020b).

Interstitial porosity and compaction trends

Interstitial porosity (ϕ_i) was obtained by correcting the total connected porosity (ϕ_t) for the clay-bound water content (ϕ_b) following Equation (2):

$$\phi_i = \phi_t - \phi_b \qquad (2)$$

The 'onboard interstitial porosity' was determined by extrapolating bound water content measured on samples to correct the total connected porosity values that were measured onboard on 153 samples at Site U1517 and 278 samples at Site U1519. At Site U1517, where extensive coring was implemented, we used onboard interstitial porosity data to determine compaction curves (Figure 7). Instead, at Site U1519 where coring was restricted to limited intervals, we used resistivity-derived porosity calibrated to onboard interstitial porosity.

Resistivity-derived porosity

For clay-rich materials, which characterised by high electrical surface conductivity, we estimated resistivity-derived porosity from LWD resistivity using the model by Revil et al. (1998). In this model, the resistivity-derived porosity (ϕ) is related to the formation factor F based on Archie's law (Archie, 1942) as expressed by Equation (3) where a and m are constants.

$$F = a\phi^{-m} \qquad (3)$$

Conin et al. (2011) and Dutilleul et al. (2020b) have shown that in siliciclastic and volcaniclastic clay-rich sediments, resistivity-derived porosity fits interstitial porosity using $a=1$ and adjusting the cementation factor (m) between 1 and 3.5.

F was determined with Equation (4) based on the bulk electrical conductivity (σ), the electrical surface conductivity (σ_s) and the electrical conductivity of the interstitial fluid (σ_{if}) as:

$$F=\frac{\sigma_{if}}{\sigma}\left[1+2\frac{\sigma_s}{\sigma_{if}}\left(\frac{\sigma_{if}}{\sigma}-1\right)\right] \quad (4)$$

since the hypotheses of Bussian (1983) and Bourlange et al. (2003) are valid at Site U1517 where $\frac{\sigma_s}{\sigma_{if}} \ll 1$.

We used ring resistivity which has the highest vertical resolution for the depth penetration (Barnes et al., 2019c) to determine σ.

σ_{if} was determined using Equation (5) from the concentrations of Cl^-, Na^+, K^+, Ca^{2+}, Mg^{2+} and SO_4^{2-} in interstitial water (C^i_{iws}) and seawater (C^i_{sw}), the ionic mobility in the fluid (β^i_f), the number of charges of ions (Z_i) and the seawater conductivity (σ_{sw}).

$$\sigma_{if}=\sigma_{sw}\frac{\sum_i\left(\beta^i_f\times Z_i\times C^i_{iws}\right)}{\sum_j\left(\beta^j_f\times Z_j\times C^j_{sw}\right)} \quad (5)$$

The seawater conductivity was calculated using Equation (6) based on temperature T (in °C).

$$\sigma_{sw}=5.32\left(1+0.02\left(T-25\right)\right) \quad (6)$$

At Site U1517, $T(°C)=5.32+39.8\times10^{-3}z$ (7) where z is the depth (in mbsf) (Barnes et al., 2019b) while $T(°C)=5.70+24.3\times10^{-3}z$ (8) at Site U1519 (Barnes et al., 2019c).

The model developed by Revil et al. (1998) assumes a major contribution of the Stern layer to surface electrical conduction, spherical grains and a linear temperature dependency of the exchangeable cation mobility (β_s) to quantify σ_s with Equation (9):

$$\sigma_s = \frac{2}{3}\rho_g CEC\,\beta_s \qquad (9)$$

Pore size distribution

Mercury injection capillary pressure (MICP)

The distribution of the size of pore throats from 360 μm to 5.7 nm was determined by MICP experiments performed with a Micromeritics® AutoPore IV 9500 at room temperature (20°C). Samples were formerly oven-dried at 105°C±5°C for 24h. During the low-pressure analysis, the samples were first degassed under vacuum. The cell was then gradually intruded by a measured volume of mercury up to a mercury pressure of ~0.2 MPa. Next, we used a high-pressure analysis sequence whereby we measured the volume of intruded mercury filling the cell and the sample at a known pressure that was increased stepwise to 220 MPa. This stage provides the distribution of the size of pore throats using the Young-Laplace Equation (10) (Purcell, 1949):

$$r = \frac{2\sigma_{Hg}\cos\theta_{Hg}}{P_{Hg}} \qquad (10)$$

from the pore throat radius (r in m), the air-mercury interfacial tension (σ_{Hg}=0.485 N/m), the mercury-sediment contact angle (θ_{Hg}=140°) and the mercury injection pressure (P_{Hg} in Pa).

Nuclear magnetic resonance (NMR)

A Bruker® Minispec Mq20 was used to perform proton NMR measurements at room temperature (20°C) and atmospheric pressure on core samples with a diameter of

8 mm. Proton NMR records the magnetisation decay of the hydrogen nuclei of water molecules in a saturated porous sample when static and pulsed magnetic fields are applied. We measured the transverse relaxation time (T_2) that provides insight into void size and porosity (Daigle et al., 2014; Bossennec et al., 2018) applying the Carr-Purcell-Meilboom-Gill (CPMG) sequence (Carr and Purcell, 1954; Meiboom and Gill, 1958). We used a recycle delay of 0.1 s, a half-echo time τ of 0.04 ms (the minimum obtainable for this equipment), gain ranging around 70–80%, 200 echoes per scan and 128 scans were stacked (Dutilleul et al., 2020b). The raw T_2 exponential decay measured was inversed in a smoothed T_2 distribution using UpenWin© software. We used the Equation (11) following Marschall et al. (1995) to correlate the T_2 (in s) measured by LWD NMR to MICP pore throat radius (here, in μm) based on the effective relaxivity (ρ_e, in μm/s):

$$r = 2\rho_e T_2 \qquad (11)$$

We extrapolated the effective relaxivity across coring gaps where no MICP data were available to determine an average pore radius profile across Sites U1517 and U1519 based on LWD NMR data.

NMR porosity ¿) (Daigle et al., 2014) was determined using Equation (12) with the volume of dry grains (V_g¿ from the helium-displacement pycnometer and the volume of water $(V¿¿w)¿$ in the sample.

$$\phi_{NMR} = \frac{V_w}{V_w + V_g} \qquad (12)$$

V_w was quantified using a calibration (Equation (13)) in which the maximum signal amplitude A_0 (corrected for the gain) was recorded during the T_2 measurement for known volume of water.

$$V_w = 19.762A_0 - 0.092 \ (R^2=0.94) \qquad (13)$$

NMR porosity was also measured onboard using the Schlumberger ProVisionPlus logging tool.

Permeability

Permeability measurements under confining pressure

Permeability measurements were conducted at room temperature, in a 200 MPa hydrostatic pressure cell equipped with a pore fluid pressure circuit (Reuschlé, 2011). Experiments were run on two cylindrical samples (20 mm in diameter and 40 mm in length) from the preslide interval at Site U1517 at 97.43 mbsf (core 17H6, lithological Unit IV) and 157.83 mbsf (core 29F3, Unit V) respectively. Permeability was measured on the initial saturated samples using a pulse decay method (Brace, 1984): an initial imposed differential pore fluid pressure (ΔP_P) is applied to equilibrate through the sample. Its decay is approximately exponential and the decay time is inversely proportional to the permeability following Equations (14) and (15) (Hsieh et al., 1981; Reuschlé, 2011):

$$\Delta P_P(t) \propto \exp(-\alpha t) \qquad (14)$$

and

$$\alpha = [Ak(C_u + C_d)]/(\mu L C_u C_d) \qquad (15)$$

with the time (*t*), the cross-sectional area (*A)* and the length (*L)* of the sample, the viscosity of the pore fluid (μ=10^{-3} Pa.s at 20°C), the permeability (*k* in m²), and the compressive storages of the upstream and downstream pore pressure circuits (C_u = 3.957×10^{-9} m^3/MPa and C_d = 4.828×10^{-9} m^3/MPa, respectively).

Permeability from mercury injection capillary pressure (MICP)

Pore throats size distribution measured by MICP was used to determine Katz-Thompson permeability K_{KT} (Katz and Thompson, 1986, 1987; Nishiyama and Yokoyama, 2014) with Equation (16):

$$K_{KT} = \frac{1}{89}\phi_i \frac{(l¿¿max^h)^3}{l_c} f\left(l^h_{max}\right)¿ \qquad (16)$$

with the pore throat diameter (l_c) at the inflection point of the cumulative MICP curve $f(l)$ of fractional volume of connected pore throats with diameters of l and larger, the pore throat diameter (l^h_{max}) corresponding to the optimum path for permeability when $l^3 f(l)$ is maximum and $l = l^h_{max}$ (Katz and Thompson, 1986, 1987).

Results

Site U1517

At Site U1517, CEC is very low to low (~0.05–0.20 mol/kg), independent of lithological units, and averages 0.15 mol/kg (Figure 4c). The range of CEC values suggests that the relatively homogeneous (~32%) total clay mineral content across the section (Figure 4b) is composed of a mix of smectite, illite, kaolinite and or/chlorite. In particular, the comparison of CEC values measured in siliciclastic clay-rich samples from the North Sumatra margin (Dutilleul et al., 2020a) and other sites from the North Hikurangi margin (e.g. Dutilleul et al., 2020b and in press) with the clay mineral assemblage determined by XRD in near-by samples (e.g. Rosenberger et al., 2020; Underwood, 2021) suggests that at Site U1517, smectite content in bulk sediment ranges ~5%-30% (Figure 8). These values agree with the post-cruise XRD characterisation of the clay mineral assemblage of Underwood and Dugan (2021). This study shows that smectite and illite contents in bulk sediment range ~5%-29% and

~5%-21% respectively while chlorite and kaolinite contents are <5% and <1% respectively (S. Cardona, pers. comm.)

Consequently, bound water content is low (~2%–8%, ~6% on average) and relatively homogeneous across the sedimentary section at Site U1517. Hence, total connected porosity and interstitial porosity show similar variation across the section drilled, in this case, an overall decrease with increasing depth (Figure 4d). However, no general compaction trend can be defined at Site U1517. In detail, interstitial porosity exponentially decreases from ~64% at the seafloor to ~34% at the base of the South TLC. The interstitial porosity versus vertical effective stress ($\sigma_v^{'}$) curve determined by least-square fitting is $\phi_i = 45.6\, e^{-0.57\sigma_v^{'}}$ (R^2=0.40, as shown in Figure 7) for the South TLC interval. A strong contrast appears with the top of lithological Unit IV where interstitial porosity is ~45% and decreases with increasing scatter following $\phi_i = 47.6\, e^{-0.14\sigma_v^{'}}$ (least-square fitting with R^2=0.23) down to ~40% at ~185 mbsf. The interstitial porosity tracks the LWD NMR porosity very well but it does not track the LWD neutron porosity which shows higher values (Figure 4d). Larger neutron porosity values are typically detected in clay-rich sediments (e.g. Expedition 314 Scientists, 2009; Expedition 317 Scientists, 2011; Expedition 334 Scientists, 2012a, b; Dutilleul et al., 2020b) due to the high concentration of hydrogen characterising the hydroxyls of the mineral structure of the clay, with a possible additional effect of trace elements acting as thermal absorbers (Ellis, 1986; Ellis and Singer, 2007). NMR porosity measured on samples generally matches LWD NMR porosity, although the latter T_2 distribution is truncated at values between 1 and 1000 ms (Barnes et al., 2019b) in contrast to laboratory measurements. An exception is Unit IV, where NMR porosity tracks LWD neutron porosity.

Overall, resistivity-derived porosity fits interstitial porosity with a =1 and m=1.7 in the TLC and m=1.9 below (Figure 4i) except in some intervals (~20–30, ~96–106, ~135-165 mbsf) as discussed below.

Figure 9 shows the permeability data obtained on cores 17H6 and 29F3 under a constant pore fluid pressure of 8 and 8.5 MPa respectively corresponding to their in-situ pore pressure conditions and an increasing effective hydrostatic confining pressure from 1 to 20 MPa. The lowest effective pressure is slightly higher than the in-situ pressure for sample 17H6 (0.87 MPa) and slightly lower for sample 29F3 (1.39 MPa). The progressive closure of cracks can explain the decrease of permeability k with effective pressure P_{eff}. Walsh (1981) proposed a fracture closure model that suggests that $k^{1/3}$ should be linearly related to log P_{eff}. Permeability plotted as $k^{1/3}$ is shown as a function of P_{eff} in a linear-log graph in Figure 10 for samples 17H6 and 29F3. The data are found to follow a linear trend, in agreement with Walsh's model. They correspond to the over-consolidation of the samples with an initially measured permeability ($1.3.10^{-18}$ m^2 for core 17H6 and $1.4.10^{-17}$ m^2 for core 29F3) close to the expected in-situ permeability.

MICP shows that the average size of pore throats decreases and is homogenised with increasing depth from 0.3 µm to 0.1 µm in lithological Units I to IV (Figure 4e). Lithological Unit V shows contrasted ranges of pore throat diameters with a general trend toward higher values, increasing up to ~1.4 µm at ~165 mbsf, and dropping down to ~0.4 µm in the lower part of the unit (Figures 4e and 11). The corresponding permeabilities determined using the Katz-Thompson model are in the order of 10^{-17} m^2. These estimated permeability values are somewhat higher than those measured under in-situ conditions (see, for example, core 17H6). The effective pressure effect may explain the difference since the Katz-Thompson estimate holds for zero pressure conditions and permeability has been shown to decrease at pressures lower than our

minimum of 1 MPa (Screaton et al., 2021). Another possible explanation may be the lower water permeability in clay- and silt-rich rocks compared to gas permeability, due to fluid-rock interactions that the Katz-Thompson model does not consider.

NMR T_2 measured on samples and LWD NMR T_2 are both well correlated to the average size of pore throats but show contrasting values (Figure 4f). NMR T_2 measured on samples are in the range of ~1–2 ms. In contrast, LWD NMR T_2 decreases from ~20 to ~6 ms from the seafloor to the bottom of Unit IV. It increases up to ~30 ms before dropping in the lower part of Unit V. The average LWD relaxivity is ~9 μm/s while the average relaxivity measured on samples is ~50 μm/s.

Site U1519

At Site U1519, CEC is low but in the high range measured at Site U1517 (~0.14–0.20 mol/kg). CEC is also independent of lithological units and averages 0.16 mol/kg (Figure 5c). This range of values suggests that the clay mineral assemblage, which constitutes ~45% of the bulk mineralogy of sediments, is homogeneous (Figure 5b). Similarly to Site U1517, the CEC values suggest that the clay fraction is composed of a mix of smectite (~5%-30% based on Figure 8), illite, kaolinite, and or/chlorite taking into account that CEC and XRD measurements were not carried out on the same samples, resulting in significant scattering (±15%). This result cannot be confirmed since no characterisation of the clay mineral assemblage was undertaken at Site U1519.

The resulting bound water content is low (~5%–8%) and relatively homogeneous across the section, averaging 7%. Hence, as observed at Site U1517, total connected porosity and interstitial porosity vary similarly (Figure 5d). Across the limited intervals where coring was attempted, the interstitial porosity decreases with increasing depth from 68% below the seafloor to ~33% at the bottom of Unit I, it shows slightly lower values at the bottom of logging and seismic Units 2 (~31%) before

405 increasing across logging and seismic Units 3 up to ~ 35% with a maximum ~42%
406 around 605 mbsf. In the first unit, strong porosity contrast occurs based on grain size,
407 with a general trend toward higher porosity values (+5% in average) in mudstones than
408 in shallower clayey siltstones/silty claystones. In contrast to Site U1517, the interstitial
409 porosity at Site U1519 is in better agreement with the LWD neutron porosity than with
410 the NMR porosity, which shows lower values. The NMR porosity measured on samples
411 exceeds the LWD NMR porosity and matches both interstitial and LWD neutron
412 porosities.

413 The resistivity-derived porosity fits the interstitial and onboard interstitial
414 porosities with a =1 and m =1.9 in lithological Unit I, m =2.3 in the lower part of
415 seismic and logging Units 2 (top of lithological Unit II), and m =2.6 in the top of
416 logging and seismic Units 3 (bottom of Unit II) except in a zone ~600–620 mbsf (Figure
417 5i). A general compaction trend $\phi_i = 39.3 e^{-0.03\sigma'_v}$ (R^2=0.16) can be defined at Site U1519
418 (excluding the washout interval ~148-227 mbsf) based on fitting the resistivity-derived
419 porosity to the onboard interstitial porosity. In detail, three different compaction trends
420 can be defined to best fit the data (Figure 7): the first one for clayey siltstones/silty
421 claystones in lithological Unit I, the second one for mudstones of the same unit, and the
422 third one for Unit II. We notice that the compaction trend for shallow clayey
423 siltstones/silty claystones in Unit I at Site U1519 determined from the onboard
424 interstitial porosity is equivalent to that of the TLC at Site U1517 where the same type
425 of lithology or even coarser lithologies have been identified.

426 MICP shows that the average size of pore throat diameters decreases and
427 becomes more homogeneous with increasing depth from ~0.45 µm to ~0.15 µm near the
428 bottom of the hole (Figures 5e and 11). As observed at Site U1517, the permeabilities
429 determined using the Katz-Thompson model are in the order of 10^{-17} m². NMR T_2

measured on samples and LWD NMR T_2 show diverging values (~10–2.30 ms and ~19–3 ms, respectively), although their evolution correlates with that of the average pore throat size measured by MICP (Figure 5e; f). The average LWD relaxivity is ~14 µm/s while the average relaxivity measured on samples is ~90 µm/s.

Discussion

Physical properties of gas hydrates bearing intervals

When not directly observed onboard, gas hydrate occurrence (green rectangle and shaded zones in Figure 4 and green rectangle in Figure 5) was inferred from 1) negative anomaly of pore water content (Figures 4j et 5j) due to gas hydrate dissociation during core retrieval (Paull and Ussler, 2001), or 2) positive peaks of LWD P-wave velocity (Figures 4g and 5g) and resistivity (Figures 4h and 5h) (Barnes et al., 2019b). However, there are uncertainties regarding the precise location of gas hydrate-bearing intervals estimated from the salinity detection method. Indeed, other phenomena, including changes in the salinity of the water mass, diagenetic reactions or the pore water extraction method used onboard may also cause negative chloride anomalies (Fitts and Brown, 1999; Barnes et al., 2019b, c; Sultan, 2020). At Site U1517, chloride data mark a zone in the preslide interval among ~135 and ~165 mbsf with gas hydrate saturation ranging 2%–68% (Barnes et al., 2019b), with the BGHS at ~162 mbsf (Screaton et al., 2019) (Figure 4). Sultan (2020) reinterpreted chloride anomalies and proposed a BGHS between 85 and 128 mbsf, although this is not supported by Screaton et al. (2019, 2020). LWD data evidenced three intervals potentially hosting gas hydrates (green shaded zones on Figure 4) between ~112–114, ~117–121 and ~128–145 mbsf (Barnes et al., 2019b). At Site U1519, chloride data mark a damage zone (Figure 5k) between 520 and 630 mbsf with elevated gas hydrate concentration with a discrete

454 negative anomaly ~628 mbsf (Figure 5j) where the occurrence of gas hydrates has been
455 directly evidenced by core IR scanning in silt layers with higher CEC at ~627 mbsf.
456 Gas hydrate distribution depends on the initial characteristics of the porous
457 medium and the effective stress that control the growing space, thus porosity and
458 permeability (Dai et al., 2012, He et al., 2013) which vary with hydrate formation and
459 dissociation (Misyura, 2016; Wang, 2020). When hydrates form in the pore space, the
460 permeability of gas hydrate saturated sediments decreases (Nimblett and Ruppel, 2003;
461 Dai and Seol, 2014; Daigle et al., 2015b; Wei et al., 2021) while it increases when
462 hydrates dissociate (Wang, 2020). Sediments characterised by a high initial porosity are
463 more sensitive to permeability changes associated with increasing gas hydrates
464 saturation (Shen et al., 2020).
465 Although there are uncertainties concerning the precise location of gas hydrate-
466 bearing intervals (e.g. Barnes et al., 2019b, c; Screaton et al., 2019 and 2020; Sultan,
467 2020), our core-based dataset shows evidence that the sediment matrix in intervals
468 likely to host gas hydrates, as inferred from chloride anomalies, is characterised by a
469 general trend of higher interstitial porosities, average pore diameters, and Katz-
470 Thompson permeabilities (Figures 4 and 5). These characteristics are favorable to the
471 growth of gas hydrates. This behaviour is more visible at Site U1517 (~135-160 mbsf)
472 than at Site U1519 (~520-630 mbsf). On LWD data, intervals hosting gas hydrates are
473 typically characterised by high electrical resistivity (Goldberg et al., 2010) and P-wave
474 velocity (Waite et al., 2009) values and apparent lower NMR porosity (Kleinberg,
475 2003). Similar values, for zones thought to host gas hydrates, can be observed at Site
476 U1517 in the intervals between ~112–114, ~117–121 and ~128–145 mbsf or in some
477 intervals at the meter scale between ~135 and 160 mbsf at Site U1517 (Figure 4h) and
478 ~520-630 mbsf at Site U1519 (Figure 5h).

Overview of the compaction state and creep mechanisms at the South TLC

Several zones at both sites show anomalously high values of resistivity-derived porosity relative to the compaction curve or the onboard interstitial porosity. Two intervals at Site U1517 (~20–30 mbsf and ~96–106 mbsf) and one at Site U1519 (~148–227 mbsf) represented by the grey shaded zones in Figures 4 and 5 with anomalously high resistivity-derived porosity correspond to washout zones (Barnes et al., 2019b, c). Peaks of high resistivity-derived porosity related to the occurrence of gas hydrates in the pore space also occur in the zone ~135-165 mbsf at Site U1517. In this section, the rapid dissociation of gas hydrates when cores are brought to the surface results in the freshening of the pore water extracted from cores, impacting resistivity-derived porosity (Barnes et al., 2019b) (Figures 4j and 5j). These zones excluded, interstitial porosity or resistivity-derived porosity can be examined to determine compaction state and discuss mechanisms behind creeping at the South TLC.

At Site U1517, interstitial porosity versus effective vertical stress curve (referred to as compaction trend) and cementation factor m vary across the TLC (~0-67 mbsf) and in the preslide interval beneath (Figure 7). In particular, although Units II and III (considered here as corresponding to the upper and lower units of the landslide) may not be genetically linked and show variations in lithology and emplacement mechanisms (Gross et al., 2018; Couvin et al., 2020; Luo et al., 2020), their porosity values plot on the same compaction trend (Figure 7). This compaction trend is similar to that of the upper sedimentary section at Site U1519, at Site U1518 nearby the deformation front (Dutilleul et al., in press), and at Site U1520 in the Hikurangi Trough (Dutilleul et al., 2020b). This suggests that mechanical compaction of shallow poorly consolidated sediments is relatively uniform across the margin, although siliciclastic lithology may slightly vary in terms of grain size between these different locations. The ‘negative

polarity intra-debris reflector' at the interface between Units II and III identified by Gross et al. (2018) (~37 mbsf, marker D in Figure 4) is not associated with an anomalously high interstitial porosity nor resistivity-derived porosity. Such anomaly was expected since this reflector has been inferred to represent an excess pore pressure zone (Gross et al., 2018) coinciding with the décollement for active creeping (Barnes et al., 2019a, b).

However, onboard interstitial porosity increases by 11% and resistivity-derived porosity by 7% at the base of the landslide at Site U1517 (~67 mbsf, marker B in Figure 4). Three hypotheses can explain the distinct porosity patterns observed in the landslide and the preslide intervals with strong porosity shift at the interface:

- Hypothesis 1: a local excess pore pressure.
- Hypothesis 2: differences in lithology, emplacement mechanisms, and deformation history result in distinct compaction trends in the landslide and preslide intervals.
- Hypothesis 3: a combination of hypotheses 1 and 2.

Hypothesis 1 is supported by the rapid burial of sediment due to the emplacement of the landslide (Screaton et al., 2019), which is likely to release fluids through rapid compaction of the preslide interval. Although our dataset does not clearly show a contrast of permeability at the base of the landslide, the clay-rich upper part of the preslide interval is prone to the accumulation of the released fluids, thus to excess pore pressure development which may also be triggered by focused fluid flow (Carey et al., 2019). On the other hand, the lithology contrast between the landslide, characterised by numerous sand and silt-rich turbidites, and the clay-rich upper part of the preslide interval supports hypothesis 2 (Gamage et al., 2011). Hypothesis 2 is also supported by the strong differences in emplacement mechanisms and thus the deformation history of

the preslide interval characterised by a mixed slope sedimentary succession (Barnes et al., 2019b) and the landslide interval. As a consequence of the quick deposition of the landslide, the preslide interval should be more consolidated than the lower landslide unit. In fact, it is less consolidated, which supports hypothesis 1. Hence, we suggest that hypothesis 3 is the most plausible.

IODP Expedition 372 drilling results and Screaton et al. (2019) have shown that gas hydrates are not involved in active creeping at the South TLC interval where they are absent. In the preslide interval where gas hydrates are expected to occur, the lack of excess pore pressure at the BGHS, evidenced by our dataset, shows that neither the hydrate dissociation model nor the hydrate pressure valve model, linking gas hydrates to slow deformation, is possible. The results of this study allow the examination of mechanisms, which are not related to gas hydrates, but may explain active creeping in the South TLC interval. Our findings support the repeated small-scale failure mechanism associated with cycles of excess pore pressure as initially proposed by Mountjoy et al. (2009), since no (hypothesis 2) or moderate (hypotheses 1 and 3) excess pore pressure is found at Site U1517 in the extensional zone of the South TLC. This mechanism could be validated in the case that a larger excess pore pressure is evidenced in the compressional zone of the landslide, which has not yet been drilled (Barnes et al., 2019a).

The sedimentary section at Site U1519 is in hydrostatic conditions. However, ~600 mbsf (~5.9 MPa in Figure 7), there is a zone where onboard interstitial porosity is 4–11% higher than the value predicted by the compaction curve of Unit II. This discrepancy of porosity values could be related to an excess pore pressure in the order of ~1.5–5 MPa. The origin of this potential excess pore pressure zone is unclear. It could be related to concentrated fluid flow in a high permeability sand-rich interval

sandwiched between lower permeability MTDs. Another possibility is a relation between the presence of free gas and the nearby location of the BGHS. However, the latter is not well constrained with, on the one hand, a possible BSR ~560 mbsf or below, and on the other hand, gas hydrates sampled in a core at ~627 mbsf (Pecher et al., 2019c).

Conclusions

We quantify interstitial porosity at the south (Site U1517) and the north (Site U1519) TLC by correcting the total connected porosity measured on core samples for bound water content determined from cation exchange capacity. At Site U1517, interstitial porosity decreases by ~30% across the TLC (~64–34%), following a compaction trend different from that of the preslide interval beneath. This porosity decrease is associated with a reduction of pore throats from ~0.3 to ~0.1 μm. At Site U1519 where coring was limited, we use the interstitial porosity to calibrate the high-resolution resistivity-derived porosity. It decreases from ~68% to ~42% following three different compaction trends, corresponding to a reduction in the average size of pore throats from ~0.45 to ~0.15 μm across the sedimentary section. At both sites, the in-situ permeability measured with a triaxial cell and deduced from pore size measurements ranges from 10^{-18} to 10^{-17} m². The dataset shows that the sedimentary intervals suspected to host gas hydrates ~112–114, ~117–121 and ~128–145 and ~135 and 160 mbsf at Site U1517 and between ~520 and 630 mbsf at Site U1519 exhibit higher interstitial porosity, pore diameter and permeability favorable to the growth of gas hydrates. These results suggest hydrostatic conditions across most of the two sedimentary sections. However, at Site U1519, excess pore pressure may occur in a zone below the base of the gas hydrate stability zone. At Site U1517, a porosity shift of ~+10% occurs at the base of the landslide. We suggest that this substantial difference in the porosity profile

between the landslide and preslide intervals results from a combination of 1) contrasted physical properties due to differences in lithology, emplacement mechanisms and compaction history and 2) moderate excess pore pressure associated with the trapping of fluids at the base of the landslide. The results of IODP Expedition 372 discredit the role of gas hydrates in active creeping at the TLC. Our results open the way to the study of other mechanisms at the TLC, such as potentially repeated small-scale failure associated with charge and discharge of excess pore pressure, or at analogous basins where submarine landslides and gas hydrates coexist. Future work, such as in situ pore pressure analysis recorded at Site U1519, is required to understand the mechanisms of creep at the TLC.

Acknowledgements

This study and the shore-based measurements were funded by CNRS-INSU and IODP-France, which we greatly acknowledge. The complete crews of IODP Expeditions 372 and 375 are sincerely thanked. We also thank David Billet, Philippe Rousselle, Maximilien Beuret and Géraldine Kitzinger from the LIEC laboratory in Nancy and Metz (France) for running CEC, exchangeable cation composition and soluble chloride content analyses. We thank Khalid Essa for his support in proofreading the manuscript. We finally thank Ann Cook and Sebastian Cardona for their very constructive reviews that greatly improved this manuscript as well as Adam McArthur for editorial handling.

Data

This research used data provided by the International Ocean Discovery Program (IODP) and freely available on the LIMS Report Interface Page at *web.iodp.tamu.edu/LORE* or on the log database at

603 *mlp.ldeo.columbia.edu/logdb/scientific_ocean_drilling*. Post-cruise data including
604 corrected porosity, CEC, exchangeable cation composition, MICP and NMR are
605 available in the OTELo Research Data Repository (https://doi.org/10.24396/ORDAR-
606 40 for Site U1519 and https://doi.org/10.24396/ORDAR-41 for Site U1517).

607 **References**

608 Alexander CR, Walsh JP, Orpin AR. 2010. Modern sediment dispersal and
609 accumulation on the outer Poverty continental margin. Marine Geology.
610 270(1):213–226. https://doi.org/10.1016/j.margeo.2009.10.015
611 Archie, G E. 1942. The electrical resistivity log as an aid in determining some reservoir
612 characteristics. Transactions of the American Institute of Mining Metallurgical
613 and Petroleum Engineers (146):54-62. https://doi.org/10.2118/942054-G
614 Barnes PM, Cheung KC, Smits AP, Almagor G, Read SAL, Barker PR, Froggatt P.
615 1991. Geotechnical analysis of the kidnappers slide, upper continental slope,
616 New Zealand. 10(1–2):159–188. https://doi.org/10.1080/10641199109379888
617 Barnes PM, Nicol A, Harrison T. 2002. Late Cenozoic evolution and earthquake
618 potential of an active listric thrust complex above the Hikurangi subduction
619 zone, New Zealand. GSA Bulletin. 114(11):1379–1405.
620 https://doi.org/10.1130/0016-7606(2002)114<1379:LCEAEP>2.0.CO;2
621 Barnes PM, Pecher IA, LeVay LJ, Bourlange SM, Brunet MMY, Cardona S, Clennell
622 MB, Cook AE, Crundwell MP, Dugan B, Elger J, Gamboa D, Georgiopoulou A,
623 Greve A, Han S, Heeschen KU, Hu G, Kim GY, Kitajima H, Koge H, Li X,
624 Machado KS, McNamara DD, Moore GF, Mountjoy JJ, Nole MA, Owari S,
625 Paganoni M, Petronotis KE, Rose PS, Screaton EJ, Shankar U, Shepherd CL,
626 Torres ME, Underwood MB, Wang X, Woodhouse AD, Wu H-Y. 2019a.
627 Expedition 372A summary. In Pecher IA, Barnes PM, LeVay LJ and the
628 Expedition 372A Scientists, Creeping Gas Hydrate Slides. Proceedings of the
629 International Ocean Discovery Program, 372A: College Station, TX
630 (International Ocean Discovery Program), https://doi.org/10.14379/
631 iodp.proc.372A.101.2019
632 Barnes PM, Pecher IA, LeVay LJ, Bourlange SM, Brunet MMY, Cardona S, Clennell
633 MB, Cook AE, Crundwell MP, Dugan B, Elger J, Gamboa D, Georgiopoulou A,

Greve A, Han S, Heeschen KU, Hu G, Kim GY, Kitajima H, Koge H, Li X, Machado KS, McNamara DD, Moore GF, Mountjoy JJ, Nole MA, Owari S, Paganoni M, Petronotis KE, Rose PS, Screaton EJ, Shankar U, Shepherd CL, Torres ME, Underwood MB, Wang X, Woodhouse AD, Wu H-Y. 2019b. Site U1517. In Pecher IA, Barnes PM, LeVay LJ and the Expedition 372A Scientists, Creeping Gas Hydrate Slides. Proceedings of the International Ocean Discovery Program, 372A: College Station, TX (International Ocean Discovery Program), https://doi.org/1014379/iodpproc372A1032019

Barnes PM, Wallace LM, Saffer DM, Pecher IA, Petronotis KE, LeVay LJ, Bell RE, Crundwell MP, Engelmann de Oliveira CH, Fagereng A, Fulton PM, Greve A, Harris RN, Hashimoto Y, Hüpers A, Ikari MJ, Ito Y, Kitajima H, Kutterolf S, Lee H, Li X, Luo M, Malie PR, Meneghini F, Morgan JK, Noda A, Rabinowitz HS, Savage HM, Shepherd CL, Shreedharan S, Solomon EA, Underwood MB, Wang M, Woodhouse AD, Bourlange SM, Brunet MMY, Cardona S, Clennell MB, Cook AE, Dugan B, Elger J, Gamboa D, Georgiopoulou A, Han S, Heeschen KU, Hu G, Kim GY, Koge H, Machado KS, McNamara DD, Moore GF, Mountjoy JJ, Nole MA, Owari S, Paganoni M, Rose PS, Screaton EJ, Shankar U, Torres ME, Wang X, Wu H-Y. 2019c. Site U1519. In Wallace LM, Saffer DM, Barnes PM, Pecher IA, Petronotis KE, LeVay LJ, and the Expedition 372/375 Scientists. Hikurangi Subduction Margin Coring, Logging, and Observatories Proceedings of the International Ocean Discovery Program, 372B/375: College Station, TX (International Ocean Discovery Program), https://doi.org/1014379/iodpproc372B3751042019

Bertrand L, Géraud Y, Diraison M. (2021). Petrophysical properties in faulted basement rocks: Insights from outcropping analogues on the West European Rift shoulders. Geothermics. 95 (102144). https://doi.org/10.1016/j.geothermics.2021.102144

Blum P. 1997. Physical properties handbook: a guide to the shipboard measurement of physical properties of deep-sea cores. ODP Tech. Note, 26. http://www-odp.tamu.edu/publications/tnotes/tn26/INDEX.HTM

Bossennec C, Géraud Y, Moretti I, Mattioni L, Stemmelen D. 2018. Pore network properties of sandstones in a fault damage zone. Journal of Structural Geology. 110:24–44. https://doi.org/10.1016/j.jsg.2018.02.003

Böttner C, Gross F, Geersen J, Crutchley GJ, Mountjoy JJ, Krastel S. 2018. Marine Forearc Extension in the Hikurangi Margin: New Insights From High-Resolution 3-D Seismic Data. Tectonics. 37(5):1472–1491. https://doi.org/10.1029/2017TC004906

Bourlange S, Henry P, Moore JC, Mikada H, Klaus A. 2003. Fracture porosity in the décollement zone of Nankai accretionary wedge using Logging While Drilling resistivity data. Earth and Planetary Science Letters. 209(1–2):103–112. https://doi.org/10.1016/S0012-821X(03)00082-7

Brown KM, Ransom B. 1996. Porosity corrections for smectite-rich sediments: Impact on studies of compaction, fluid generation, and tectonic history. Geology. 24(9):843–846. https://doi.org/10.1130/0091-7613(1996)024<0843:PCFSRS>2.3.CO;2

Bussian AE. 1983. Electrical conductance in a porous medium. Geophysics. 48(9):1258–1268. https://doi.org/10.1190/1.1441549

Brace WF. 1984. Permeability of crystalline rocks: new in situ measurements. Journal of Geophysical Research: Solid Earth. 89(B6):4327–4330. https://doi.org/10.1029/JB089iB06p04327

Canals M, Lastras G, Urgeles R, Casamor JL, Mienert J, Cattaneo A, De Batist M, Haflidason H, Imbo Y, Laberg JS, Locat J, Long D, Longva O, Masson DG, Sultan N, Trincardi R, Bryn P. 2004. Slope failure dynamics and impacts from seafloor and shallow sub-seafloor geophysical data: case studies from the COSTA project. COSTA - Continental Slope Stability 213(1):9-72. https://doi.org/10.1016/j.margeo.2004.10.001

Carey JM, Crutchley GJ, Mountjoy JJ, Petley DN, McSaveney MJ, Lyndsell B. 2019. Slow episodic movement driven by elevated pore-fluid pressures in shallow subaqueous slopes. Geomorphology. 329:99–107. https://doi.org/10.1016/j.geomorph.2018.12.034

Carr HY, Purcell EM. 1954. Effects of diffusion on free precession in nuclear magnetic resonance experiments. Physical Review. 94(3):630–638. https://doi.org/10.1103/PhysRev.94.630

Conin M, Henry P, Bourlange S, Raimbourg H, Reuschlé T. 2011. Interpretation of porosity and LWD resistivity from the Nankai accretionary wedge in light of

clay physicochemical properties: Evidence for erosion and local overpressuring. Geochemistry, Geophysics, Geosystems. 12(3). https://doi.org/10.1029/2010GC003381

Couvin B, Georgiopoulou A, Mountjoy JJ, Amy L, Crutchley GJ, Brunet M, Cardona S, Gross F, Böttner C, Krastel S, Pecher I. 2020. A new depositional model for the Tuaheni Landslide Complex, Hikurangi Margin, New Zealand. Geological Society, London, Special Publications. 500(1):551–566. https://doi.org/10.1144/SP500-2019-180

Dai S, Santamarina JC, Waite WF, Kneafsey TJ. 2012. Hydrate morphology: Physical properties of sands with patchy hydrate saturation, Journal of Geophysical Research: Solid Earth. 117(B11205). https://doi.org/10.1029/2012JB009667.

Dai S, Seol Y. 2014. Water permeability in hydrate-bearing sediments: a pore-scale study. Geophysical Research Letters. 41(12): 4176–4184. https://doi.org/10.1002/2014GL060535

Daigle H, Thomas B, Rowe H, Nieto M. 2014. Nuclear magnetic resonance characterization of shallow marine sediments from the Nankai Trough, Integrated Ocean Drilling Program Expedition 333: NMR of Nankai Trough sediments. Journal of Geophysical Research: Solid Earth. 119(4):2631–2650. https://doi.org/10.1002/2013JB010784

Daigle H, Ghanbarian B, Henry P, Conin M. 2015a. Universal scaling of the formation factor in clays: Example from the Nankai Trough. Journal of Geophysical Research: Solid Earth. 120(11):7361–7375. https://doi.org/10.1002/2015JB012262

Daigle H, Cook A, Malinverno A. 2015b. Permeability and porosity of hydrate-bearing sediments in the northern Gulf of Mexico. Marine and Petroleum Geology. 68(A):551-564. https://doi.org/10.1016/j.marpetgeo.2015.10.004

Dutilleul J, Bourlange S, Conin M, Géraud Y. 2020. Quantification of bound water content, interstitial porosity and fracture porosity in the sediments entering the North Sumatra subduction zone from Cation Exchange Capacity and IODP Expedition 362 resistivity data. Marine and Petroleum Geology. 111:156–165. https://doi.org/10.1016/j.marpetgeo.2019.08.007

Dutilleul J, Bourlange S, Géraud Y, Stemmelen D. 2020. Porosity, Pore Structure, and Fluid Distribution in the Sediments Entering the Northern Hikurangi Margin,

New Zealand. Journal of Geophysical Research: Solid Earth. 125(11). https://doi.org/10.1029/2020JB020330

Dutilleul J, Bourlange S, Geraud Y. In Press. Porosity and compaction state at the active Pāpaku thrust fault in the frontal accretionary wedge of the Northern Hikurangi margin. Geochemistry, Geophysics, Geosystems. https://doi.org/10.1029/2020GC009325

Ellis DV. 1986. Neutron porosity devices—what do they measure? First Break.4(3):11–17. https://doi.org/10.3997/1365-2397.1986005

Ellis DV, Singer JM. 2007. Well logging for earth scientists. 2nd ed. Dordrecht, The Netherlands: Springer.

Expedition 314 Scientists, 2009. Expedition 314 Site C0002. In Kinoshita, M., Tobin, H., Ashi, J., Kimura, G., Lallemant, S., Screaton, E.J., Curewitz, D., Masago, H., Moe, K.T., and the Expedition 314/315/316 Scientists, Proc. IODP, 314/315/316: Washington, DC (Integrated Ocean Drilling Program Management International, Inc.). https://doi.org/10.2204/iodp.proc.314315316.114.2009

Expedition 317 Scientists, 2011. Site U1352. In Fulthorpe, C.S., Hoyanagi, K., Blum, P., and the Expedition 317 Scientists, Proc. IODP, 317: Tokyo (Integrated Ocean Drilling Program Management International, Inc.). https://doi.org/10.2204/iodp.proc.317.104.2011

Expedition 334 Scientists, 2012a. Site U1378. In Vannucchi, P., Ujiie, K., Stroncik, N., Malinverno, A., and the Expedition 334 Scientists, Proc. IODP, 334: Tokyo (Integrated Ocean Drilling Program Management International, Inc.). https://doi.org/10.2204/iodp.proc.334.103.2012

Expedition 334 Scientists, 2012b. Site U1379. In Vannucchi, P., Ujiie, K., Stroncik, N., Malinverno, A., and the Expedition 334 Scientists, Proc. IODP, 334: Tokyo (Integrated Ocean Drilling Program Management International, Inc.). https://doi.org/10.2204/iodp.proc.334.104.2012

Field BD, Uruski CI, Beu AG, Browne GH, Crampton JS, Funnell RH, Killops SD, Laird M, Mazengarb C, Morgans HEG, Rait GJ, Smale D, Strong CP. 1997. Cretaceous-Cenozoic geology and petroleum systems of the East Coast region, New Zealand. Lower Hutt: Institute of Geological & Nuclear Sciences. Institute of Geological & Nuclear Sciences monograph 19 2 v.

764 Fitts TG, Brown KM. 1999. Stress-induced smectite dehydration: ramifications for
765 patterns of freshening and fluid expulsion in the N. Barbados accretionary
766 wedge. Earth and Planetary Science Letters. 172(1–2):179–197.
767 https://doi.org/10.1016/S0012-821X(99)00168-5
768 Freed R, Peacor D. 1989.Geopressured Shale and Sealing Effect of Smectite to Illite
769 Transition. AAPG Bulletin 73: 1223-1232.
770 Gamage K, Screaton, E, Bekins B, Aiello I. 2011. Permeability–porosity relationships
771 of subduction zone sediments. Marine Geology. 279: 19-36.
772 https://doi.org/10.1016/j.margeo.2010.10.010.
773 Goldberg D, Kleinberg R, Weinberger J, Malinverno A, McLellan P, Collett T. 2010.
774 16. Evaluation of natural gas-hydrate systems using borehole logs, in
775 Geophysical Characterization of Gas Hydrates, edited by M. Riedel, E. C.
776 Willoughby, and S. Chopra, pp. 239–261, Society of Exploration Geophysicists,
777 Tulsa, Okla.
778 Gross F, Mountjoy JJ, Crutchley GJ, Böttner C, Koch S, Bialas J, Pecher I, Woelz S,
779 Dannowski A, Micallef A, et al. 2018. Free gas distribution and basal shear zone
780 development in a subaqueous landslide – Insight from 3D seismic imaging of
781 the Tuaheni Landslide Complex, New Zealand. Earth and Planetary Science
782 Letters. 502:231–243. https://doi.org/10.1016/j.epsl.2018.09.002
783 He J, Liu X, Yu Z et al. 2013. Factors influencing the porosity of gas hydrate bearing
784 sediments. Science China Earth Sciences. 56:557–567. https://doi-org.bases-
785 doc.univ-lorraine.fr/10.1007/s11430-012-4452-x
786 Henry P. 1997. Relationship between Porosity, Electrical Conductivity, and Cation
787 Exchange Capacity in Barbados wedge Sediments. Proceedings of the Ocean
788 Drilling Program, Scientific Results. 156:137-150
789 https://doi.org/10.2973/odp.proc.sr.156.020.1997.
790 Henry P, Bourlange S. 2004. Smectite and fluid budget at Nankai ODP sites derived
791 from cation exchange capacity. Earth and Planetary Science Letters. 219(1–
792 2):129–145. https://doi.org/10.1016/S0012-821X(03)00694-0
793 Hsieh PA, Tracy JV, Neuzil CE, Bredehoeft JD, Silliman SE. 1981. A transient
794 laboratory method for determining the hydraulic properties of ‘tight’ rocks—I.
795 Theory. International Journal of Rock Mechanics and Mining Sciences &

Geomechanics Abstracts. 18(3):245–252. https://doi.org/10.1016/0148-9062(81)90979-7

Kastner M, Solomon EA, Harris RN, Torres ME. 2014. Chapter 4.4.3 - Fluid Origins, Thermal Regimes, and Fluid and Solute Fluxes in the Forearc of Subduction Zones. In: Stein R, Blackman DK, Inagaki F, Larsen H-C, editors. Developments in Marine Geology. Vol. 7. Elsevier; p. 671–733. https://doi.org/10.1016/B978-0-444-62617-2.00022-0

Katz AJ, Thompson AH. 1986. Quantitative prediction of permeability in porous rock. Physical Review B. 34(11):8179–8181. https://doi.org/10.1103/PhysRevB.34.8179

Katz AJ, Thompson AH. 1987. Prediction of rock electrical conductivity from mercury injection measurements. Journal of Geophysical Research. 92(B1):599. https://doi.org/10.1029/JB092iB01p00599

Kleinberg RL, Flaum C, Straley, C, Brewer, PG, Malby, GE, Peltzer, ET, III, Freiderich, G, Yesinowski, JP, 2003. Seafloor nuclear magnetic resonance assay of methane hydrate in sediment and rock. Journal of Geophysical Research: Solid Earth, 108(B3):2137. https://doi.org/10.1029/2001JB000919

Kuhlmann J, Orpin AR, Mountjoy JJ, Crutchley GJ, Henrys S, Lunenburg R, Huhn K. 2019. Seismic and lithofacies characterization of a gravity core transect down the submarine Tuaheni Landslide Complex, NE New Zealand. Geological Society, London, Special Publications. 477(1):479–495. https://doi.org/10.1144/SP477.37

Luo M, Torres ME, Kasten S, Mountjoy JJ. 2020. Constraining the Age and Evolution of the Tuaheni Landslide Complex, Hikurangi Margin, New Zealand, Using Pore-Water Geochemistry and Numerical Modeling. Geophysical Research Letters. 47(11). https://doi.org/10.1029/2020GL087243

Marschall D, Gardner JS, Mardon D, Coates R. 1995. Method for Correlating NMR Relaxometry and Mercury injection Data. Paper Number 9511 presented at: SCA Conference.

McNeill LC, Dugan B, Petronotis KE, Backman J, Bourlange S, Chemale F, Chen W, Colson TA, Frederik MCG, Guèrin G, Hamahashi M, Henstock T, House BM, Hüpers A, Jeppson TN, Kachovich S, Kenigsberg AR, Kuranaga M, Kutterolf S,

Milliken KL, Mitchison FL, Mukoyoshi H, Nair N, Owari S, Pickering KT, Pouderoux HFA, Yehua S, Song I, Torres ME, Vannucchi P, Vrolijk PJ, Yang T, Zhao X, 2017a. Site U1480. In McNeill LC, Dugan B, Petronotis KE, and the Expedition 362 Scientists, Sumatra Subduction Zone. Proceedings of the International Ocean Discovery Program, 362: College Station, TX (International Ocean Discovery Program). https://doi.org/10.14379/iodp.proc.362.103.2017

McNeill LC, Dugan B, Petronotis KE, Backman J, Bourlange S, Chemale F, Chen W, Colson TA, Frederik MCG, Guèrin G, Hamahashi M, Henstock T, House BM, Hüpers,A, Jeppson TN, Kachovich S, Kenigsberg AR, Kuranaga M, Kutterolf S, Milliken,KL, Mitchison FL, Mukoyoshi H, Nair N, Owari S, Pickering,KT, Pouderoux HFA, Yehua S, Song I, Torres ME, Vannucchi P, Vrolijk PJ, Yang T, Zhao, X. 2017b. Site U1481. In McNeill LC, Dugan B, Petronotis KE, and the Expedition 362 Scientists, Sumatra Subduction Zone. Proceedings of the International Ocean Discovery Program, 362: College Station, TX (International Ocean Discovery Program). https://doi.org/10.14379/iodp.proc.362.104.2017

Meiboom S, Gill D. 1958. Modified Spin-Echo Method for Measuring Nuclear Relaxation Times. Review of Scientific Instruments. 29(8):688–691. https://doi.org/10.1063/1.1716296

Misyura, S. 2016. The influence of porosity and structural parameters on different kinds of gas hydrate dissociation. Science Report 6, 30324. https://doi.org/10.1038/srep30324

Moore JC, Vrolijk P. 1992. Fluids in accretionary prisms. Reviews of Geophysics. 30(2):113. https://doi.org/10.1029/92RG00201

Mountjoy JJ, McKean J, Barnes PM, Pettinga JR. 2009. Terrestrial-style slow-moving earthflow kinematics in a submarine landslide complex. Marine Geology. 267(3–4):114–127. https://doi.org/10.1016/j.margeo.2009.09.007

Mountjoy JJ, Barnes PM. 2011. Active upper plate thrust faulting in regions of low plate interface coupling, repeated slow slip events, and coastal uplift: Example from the Hikurangi Margin, New Zealand. Geochemistry, Geophysics, Geosystems. 12(1). https://doi.org/10.1029/2010GC003326

Mountjoy J, Pecher I, Henrys S, Barnes P, Plaza-Faverola A. 2013. Creeping deformation mechanisms for mixed hydrate-sediment submarine landslides. In: EGU General Assembly Conference Abstracts. EGU2013-3489.

Mountjoy JJ, Pecher I, Henrys S, Crutchley G, Barnes PM, Plaza-Faverola A. 2014. Shallow methane hydrate system controls ongoing, downslope sediment transport in a low-velocity active submarine landslide complex, Hikurangi Margin, New Zealand. Geochemistry, Geophysics, Geosystems. 15(11):4137–4156. https://doi.org/10.1002/2014GC005379

Mulder T, Cochonat P. 1996. Classification of offshore mass movements. Journal ofSedimentary Research 66, 43–57. https://doi.org/10.1306/D42682AC-2B26-11D7-8648000102C1865D

Nimblett J, Ruppel C. 2003. Permeability evolution during the formation of gas hydrates in marine sediments. Journal of Geophysical Research: Solid Earth. 108(B8):2420-2003. https://doi.org/10.1029/2001JB001650

Nishiyama N, Yokoyama T. 2014. Estimation of permeability of sedimentary rocks by applying water-expulsion porosimetry to Katz and Thompson model. Engineering Geology. 177:75–82. https://doi.org/10.1016/j.enggeo.2014.05.016

Paull CK, Ussler W, III, 2001. History and significance of gas sampling during DSDP and ODP drilling associated with gas hydrates. In Paull, C.K., and Dillon, W.P. (Eds.), Natural Gas Hydrates: Occurrence, Distribution, and Detection. Geophysical Monograph, 124:53–66. https://doi.org/10.1029/GM124p0053

Pecher IA, Mountjoy JJ, Crutchley G, Henrys S, Torres ME, Huhn K, Kukowski N, Santamarina C, Riedel M, Strasser M, Bialas J, Krastel S, Vanneste M. 2014. Creeping Gas Hydrate Slides: Slow Deformation of Submarine Landslides on the Hikurangi Margin. IODP Original proposal 841-Apl2.

Pecher IA, Barnes PM, LeVay LJ, Bourlange SM, Brunet MMY, Cardona S, Clennell MB, Cook AE, Crundwell MP, Dugan B, Elger J, Gamboa D, Georgiopoulou A, Greve A, Han S, Heeschen KU, Hu G, Kim GY, Kitajima H, Koge H, Li X, Machado KS, McNamara DD, Moore GF, Mountjoy JJ, Nole MA, Owari S, Paganoni M, Petronotis KE, Rose PS, Screaton EJ, Shankar U, Shepherd CL, Torres ME, Underwood MB, Wang X, Woodhouse AD, Wu H-Y. 2019. Expedition 372A methods. In: Pecher IA, Barnes PM, LeVay LJ and the Expedition 372A Scientists, Creeping Gas Hydrate Slides. Proceedings of the International Ocean Discovery Program, 372A: College Station, TX (International Ocean Discovery Program). https://doi.org/10.14379/iodp.proc.372A.102.2019

Pedley KL, Barnes PM, Pettinga JR, Lewis KB. 2010. Seafloor structural geomorphic evolution of the accretionary frontal wedge in response to seamount subduction, Poverty Indentation, New Zealand. Marine Geology. 270(1–4):119–138. https://doi.org/10.1016/j.margeo.2009.11.006

Purcell WR. 1949. Capillary Pressures - Their Measurement Using Mercury and the Calculation of Permeability Therefrom. Journal of Petroleum Technology. 1(02):39–48. https://doi.org/10.2118/949039-G

Reuschlé T, 2011. Data report: permeability measurements under confining pressure, Exp. 315 and 316, Nankai Trough. In: Kinoshita M, Tobin H, Ashi J, Kimura G, Lallemant S, Screaton EJ, Curewitz D, Masago H, Moe KT and the Expedition 314/315/316 Scientists, Proceedings of the Integrated Ocean Drilling Program, 314/315/316: Washington, DC, https://doi.org/10.2204/iodp.proc.314315316.205.2011.

Revil A, Cathles LM, Losh S, Nunn JA. 1998. Electrical conductivity in shaly sands with geophysical applications. Journal of Geophysical Research: Solid Earth. 103(B10):23925–23936. https://doi.org/10.1029/98JB02125

Rosenberger K, Underwood, MB, Vrolijk P, Haines S. 2020. Data report: clay mineral assemblages in hemipelagic sediments entering the Sumatra subduction zone, IODP Sites U1480 and U1481, Expedition 362. In McNeill LC, Dugan B, Petronotis KE, and the Expedition 362 Scientists. Sumatra Subduction Zone. Proceedings of the International Ocean Discovery Program, 362: College Station, TX (International Ocean Discovery Program). https://doi.org/10.14379/iodp.proc.362.204.2020

Saffer DM, Wallace LM, Barnes PM, Pecher IA, Petronotis KE, LeVay LJ, Bell RE, Crundwell MP, Engelmann de Oliveira CH, Fagereng A, Fulton PM, Greve A, Harris RN, Hashimoto Y, Hüpers A, Ikari MJ, Ito Y, Kitajima H, Kutterolf S, Lee H, Li X, Luo M, Malie PR, Meneghini F, Morgan JK, Noda A, Rabinowitz HS, Savage HM, Shepherd CL, Shreedharan S, Solomon EA, Underwood MB, Wang M, Woodhouse AD, Bourlange SM, Brunet MMY, Cardona S, Clennell MB, Cook AE, Dugan B, Elger J, Gamboa D, Georgiopoulou A, Han S, Heeschen KU, Hu G, Kim GY, Koge H, Machado KS, McNamara DD, Moore GF, Mountjoy JJ, Nole MA, Owari S, Paganoni M, Rose PS, Screaton EJ,

Shankar U, Torres ME, Wang X, Wu H-Y. 2019. Expedition 372B/375 summary. https://doi.org/10.14379/iodp.proc.372B375.101.2019

Screaton E, Saffer D, Henry P, Hunze S. 2002. Porosity loss within the underthrust sediments of the Nankai accretionary complex: Implications for overpressures. Geology. 30(1):19. https://doi.org/10.1130/0091-7613(2002)030<0019:PLWTUS>2.0.CO;2

Screaton, E.J., Torres, M.E., Dugan, B., Heeschen, K.U., Mountjoy, J.J., Ayres, C., Rose, P.S., Pecher, I.A., Barnes, P.M., and LeVay, L.J. (2019). Sedimentation Controls on Methane-Hydrate Dynamics Across Glacial/Interglacial Stages: An Example From International Ocean Discovery Program Site U1517, Hikurangi Margin. Geochemistry, Geophysics, Geosystems. 20 (11):4906-4921. https://doi.org/10.1029/2019GC008603.

Screaton EJ, Torres ME, Dugan B, Heeschen KU, Mountjoy JJ, Ayres C, Rose PS, Pecher IA, Barnes PM, LeVay LJ. 2020. Reply to Comments by N. Sultan on "Sedimentation Controls on Methane-Hydrate Dynamics Across Glacial/Interglacial Stages: An Example From International Ocean Discovery Program Site U1517, Hikurangi Margin." Geochemistry, Geophysics, Geosystems. 21(6). https://doi.org/10.1029/2020GC009005

Screaton EJ, Summerfield C, Jaeger JM, Whipple J. 2021. Data report: permeability and grain size of sediments, IODP Expeditions 372 and 375. In: Wallace LM, Saffer DM, Barnes PM, Pecher IA, Petronotis KE, LeVay LJ and the Expedition 372/375 Scientists, Hikurangi Subduction Margin Coring and Observatories. Proceedings of the International Ocean Discovery Program, 372B/375: College Station, TX (International Ocean Discovery Program) https://doi.org/10.14379/iodp.proc.372B375.205.2021

Shen P, Li G, Li B, Li X. 2020. Coupling effect of porosity and hydrate saturation on the permeability of methane hydrate-bearing sediments. Fuel. 269. 117425. https://doi.org/10.1016/j.fuel.2020.117425

Sultan N. 2020. Comment on "Sedimentation Controls on Methane-Hydrate Dynamics Across Glacial/Interglacial Stages: An Example From International Ocean Discovery Program Site U1517, Hikurangi Margin" by E. J. Screaton et al. Geochemistry, Geophysics, Geosystems. 21(6). https://doi.org/10.1029/2019GC008846

Underwood MB, Dugan B, 2021. Data report: clay mineral assemblages within and beneath the Tuaheni landslide complex, IODP Site U1517, offshore New Zealand. In Pecher I.A, Barnes PM, LeVay LJ and the Expedition 372A Scientists, Creeping Gas Hydrate Slides. Proceedings of the International Ocean Discovery Program, 372A: College Station, TX (International Ocean Discovery Program). https://doi.org/10.14379/iodp.proc.372A.201.2021

Underwood MB. 2021. Data report: clay mineral assemblages within trench-floor and accreted trench-floor deposits, IODP Expedition 372B/375 Sites U1518 and U1520, offshore New Zealand. In Wallace LM, Saffer DM, Barnes PM, Pecher IA, Petronotis KE, LeVay LJ and the Expedition 372/375 Scientists, Hikurangi Subduction Margin Coring, Logging, and Observatories. Proceedings of the International Ocean Discovery Program, 372B/375: College Station, TX (International Ocean Discovery Program). https://doi.org/10.14379/iodp.proc.372B375.206.2021

Underwood MB, Dugan B. 2021. Data report: clay mineral assemblages within and beneath the Tuaheni Landslide Complex, IODP Expedition 372A Site U1517, offshore New Zealand. In Pecher, I.A., Barnes, P.M., LeVay, L.J., and the Expedition 372A Scientists, Creeping Gas Hydrate Slides. Proceedings of the International Ocean Discovery Program, 372A: College Station, TX (International Ocean Discovery Program). https://doi.org/10.14379/iodp.proc.372A.201.2021

Waite WF et al. 2009. Physical properties of hydrate-bearing sediments, Reviews of Geophysics. 47, RG4003, https://doi.org/10.1029/2008RG000279.

Wallace LM, Beavan J, McCaffrey R, Desmond D. 2004. Subduction zone coupling and tectonic block rotations in the North Island, New Zealand. Journal of Geophysical Research. 109(B12). https://doi.org/10.1029/2004JB003241

Wallace LM, Saffer DM, Barnes PM, Pecher IA, Petronotis KE, LeVay LJ, Bell RE, Crundwell MP, Engelmann de Oliveira CH, Fagereng A, Fulton PM, Greve A, Harris RN, Hashimoto Y, Hüpers A, Ikari MJ, Ito Y, Kitajima H, Kutterolf S, Lee H, Li X, Luo M, Malie PR, Meneghini F, Morgan JK, Noda A, Rabinowitz HS, Savage HM, Shepherd CL, Shreedharan S, Solomon EA, Underwood MB, Wang M, Woodhouse AD, Bourlange SM, Brunet MMY, Cardona S, Clennell MB, Cook AE, Dugan B, Elger J, Gamboa D, Georgiopoulou A, Han S,

Heeschen KU, Hu G, Kim GY, Koge H, Machado KS, McNamara DD, Moore GF, Mountjoy JJ, Nole MA, Owari S, Paganoni M, Rose PS, Screaton EJ, Shankar U, Torres ME, Wang X, Wu, H-Y. 2019. Expedition 372B/375 methods, https://doi.org/10.14379/iodp.proc.372B375.102.2019

Walsh JB. 1981. Effect of pore pressure and confining pressure on fracture permeability. International Journal of Rock Mechanics and Mining Sciences & Geomechanics Abstracts, 18:429-435, https://doi.org/10.1016/0148-9062(81)90006-1.

Wang L, Gu LJ, Lu HL. 2020. Sediment permeability change on natural gas hydrate dissociation induced by depressurization. China Geology 3(2):221-229. https://doi.org/10.31035/cg2020039

Wei J, Wu T, Feng X, Liang J, Li W, Xie R, Wu G. 2021.Physical Properties of Gas Hydrate-Bearing Pressure Core Sediments in the South China Sea. Geofluids. https://doi.org/10.1155/2021/6636125

Figures

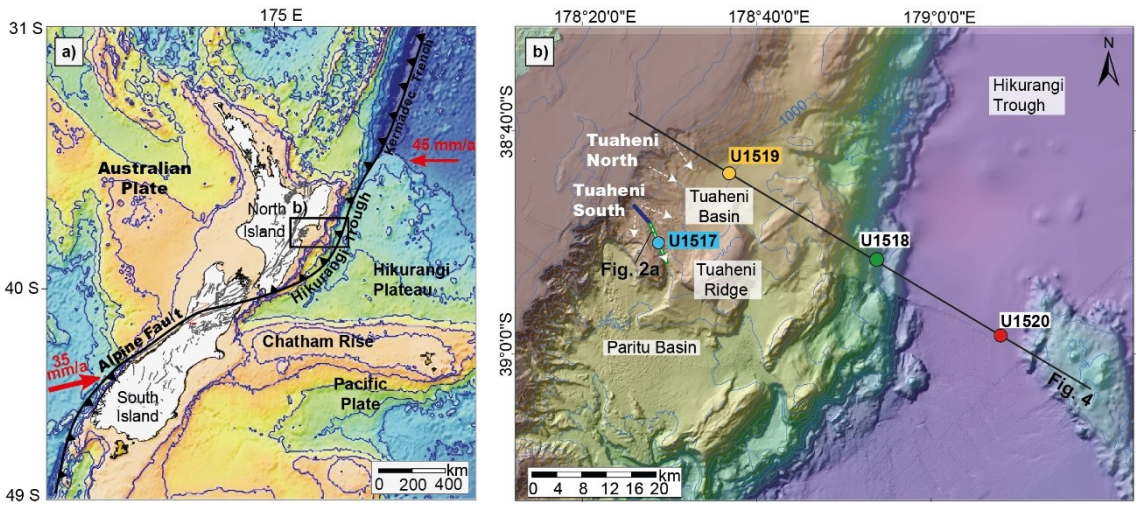

Figure 1. a) Tectonic setting of the Hikurangi margin with plate motion indicated by red arrows (modified after Barnes et al., 2019a). b) Bathymetric map of the IODP Expeditions 372/375 study area offshore Gisborne located on a) (modified after Mountjoy et al., 2014 and Saffer et al., 2019). The thick line represents the seismic profile TAN1114-10b shown in Figure 2a with the location of Site U1517. The blue (respectively, green) section of this line indicates the contractional (respectively, extensional) zone of the slide represented in Figure 2a. The black line represents the seismic profile 05CM-04 across the margin with the location of Site U1519 and of other Sites from IODP Expeditions 372-375. White dashed arrows display the direction of movement within the landslides of the North and South Tuaheni (after Mountjoy et al., 2014).

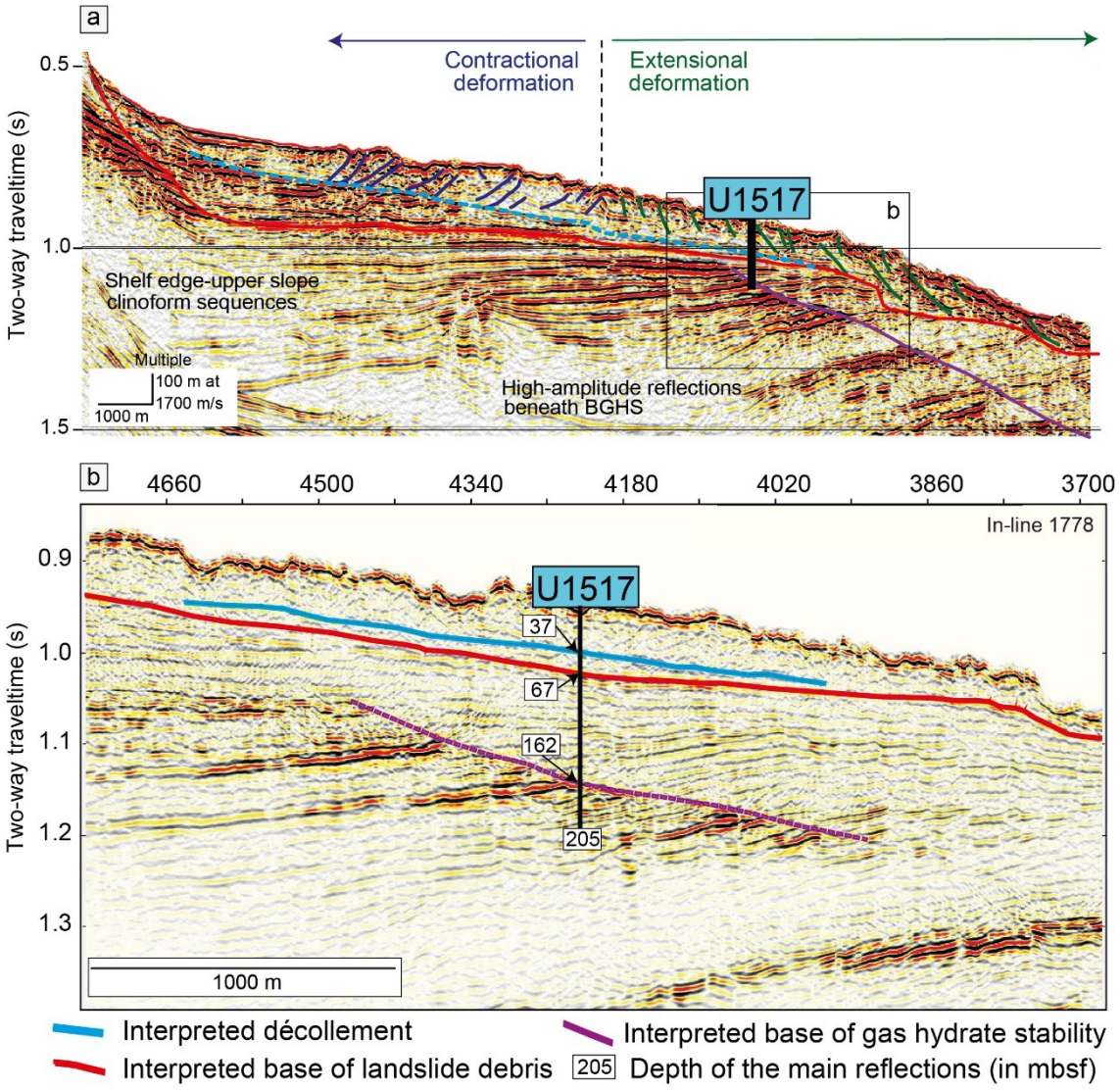

1020

1021 Figure 2. a) Seismic profile TAN1114-10b across the South Tuaheni landslide
1022 (modified after Mountjoy et al., 2014 and Barnes et al., 2019a) with b) a zoom in on
1023 Site U1517 in the extensional part and the main seismic reflectors (in-line 1778), with
1024 the depth in metres below sea floor (modified after Barnes et al., 2019a). BGHS: base of
1025 the gas hydrate stability zone.

1026

1027

1028

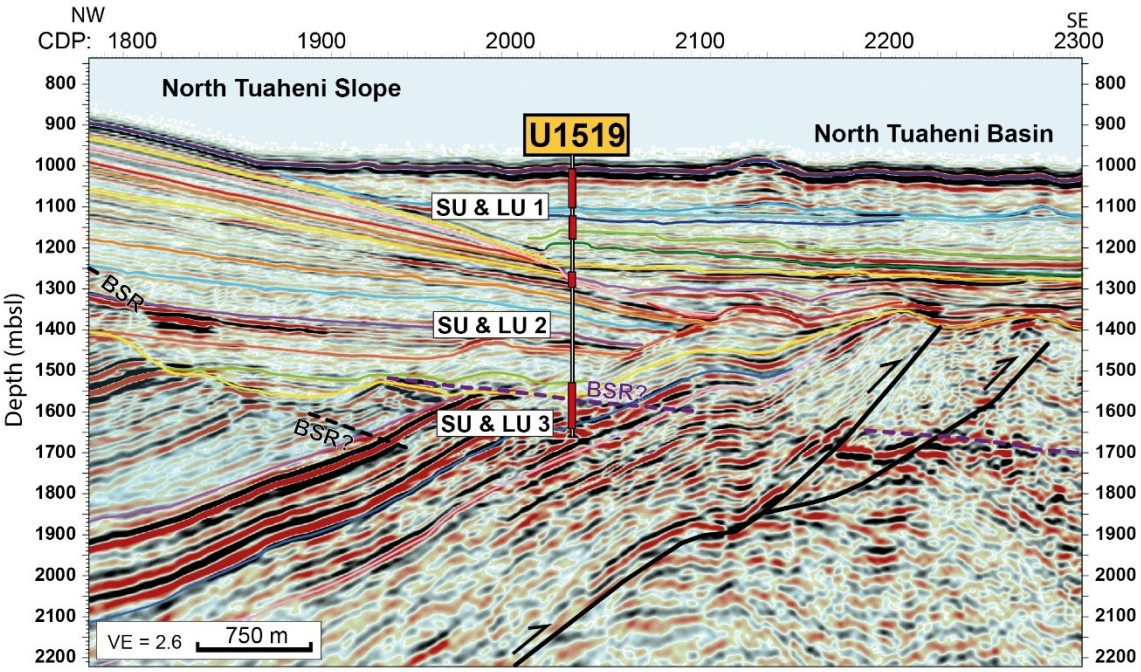

1029

1030 Figure 3. Zoom in on seismic profile 05CM-04 (Figure 1b) on Site U1519 showing the

1031 cored sections (red bars), logging units (LU) and seismic units (SU) (modified after

1032 Barnes et al., 2019c). VE: vertical exaggeration; BSR: bottom-simulating-reflector.

1033

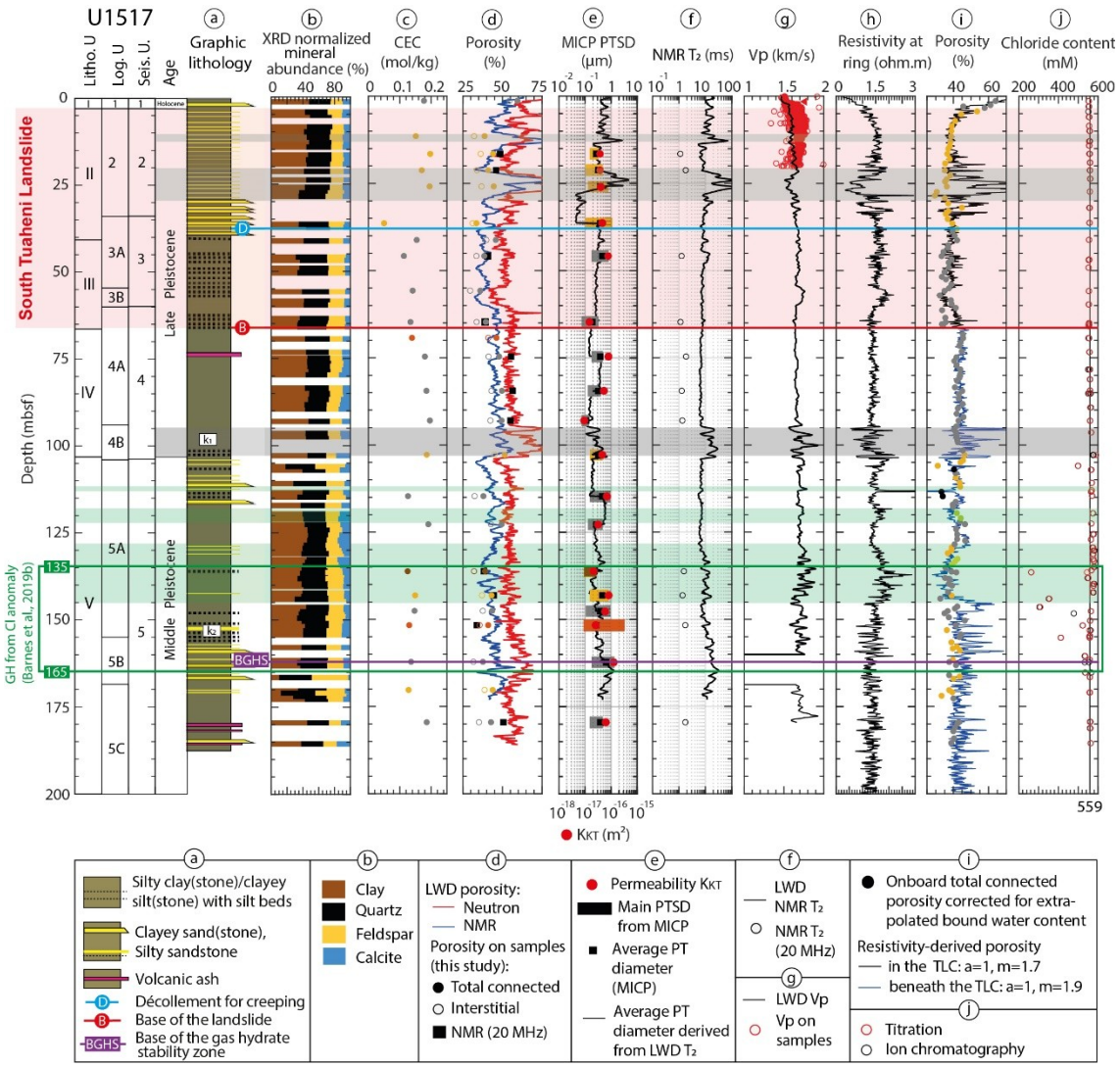

Figure 4. Summary of lithological, logging and seismic units and description (a), mineralogical (b), chemical (c and j) and physical (d, e, f, g, h, i) properties at Site U1517. For (c), (d), (e) and (i), the colour of data points or bars indicates the lithology of the samples analysed: light green for clay(stone); black for silt(stone); gold for alternating sand(stone) and mud(stone) layers; grey for silty clay(stone), clayey silt(stone) or alternating silt and clay layers; orange for clayey silt(stone) with sand; brown for silt(stone) with sand. k_1 and k_2 indicate the location of cores 17H6 and 29F3 respectively for permeability measurements. XRD: X-Ray diffraction; CEC: Cation exchange capacity; Kkt: Katz–Thompson permeability; MICP PT(SD): mercury injection capillary pressure pore throat (size distribution) determined based on Bertrand

et al. (2021); NMR: nuclear magnetic resonance; T_2: transverse relaxation time; LWD: logging-while-drilling; Vp: P-wave velocity; TLC: Tuaheni Landslide Complex. The red shaded zone represents the landslide mass with marker horizons D and B. The three green shaded zones highlight zones expected to host gas hydrates based on LWD data. The green rectangle indicates the zone hosting gas hydrates from chloride anomalies (Barnes et al., 2019b). In j), 559 mM is the average chloride concentration in modern seawater. The base of the gas hydrate stability zone (BGHS) is located at 162 mbsf (Screaton et al., 2019). The grey shaded zones are interpreted onboard as washout zones between ~10-13 mbsf, ~21-28 mbsf and ~94-104 mbsf (Barnes et al., 2019a).

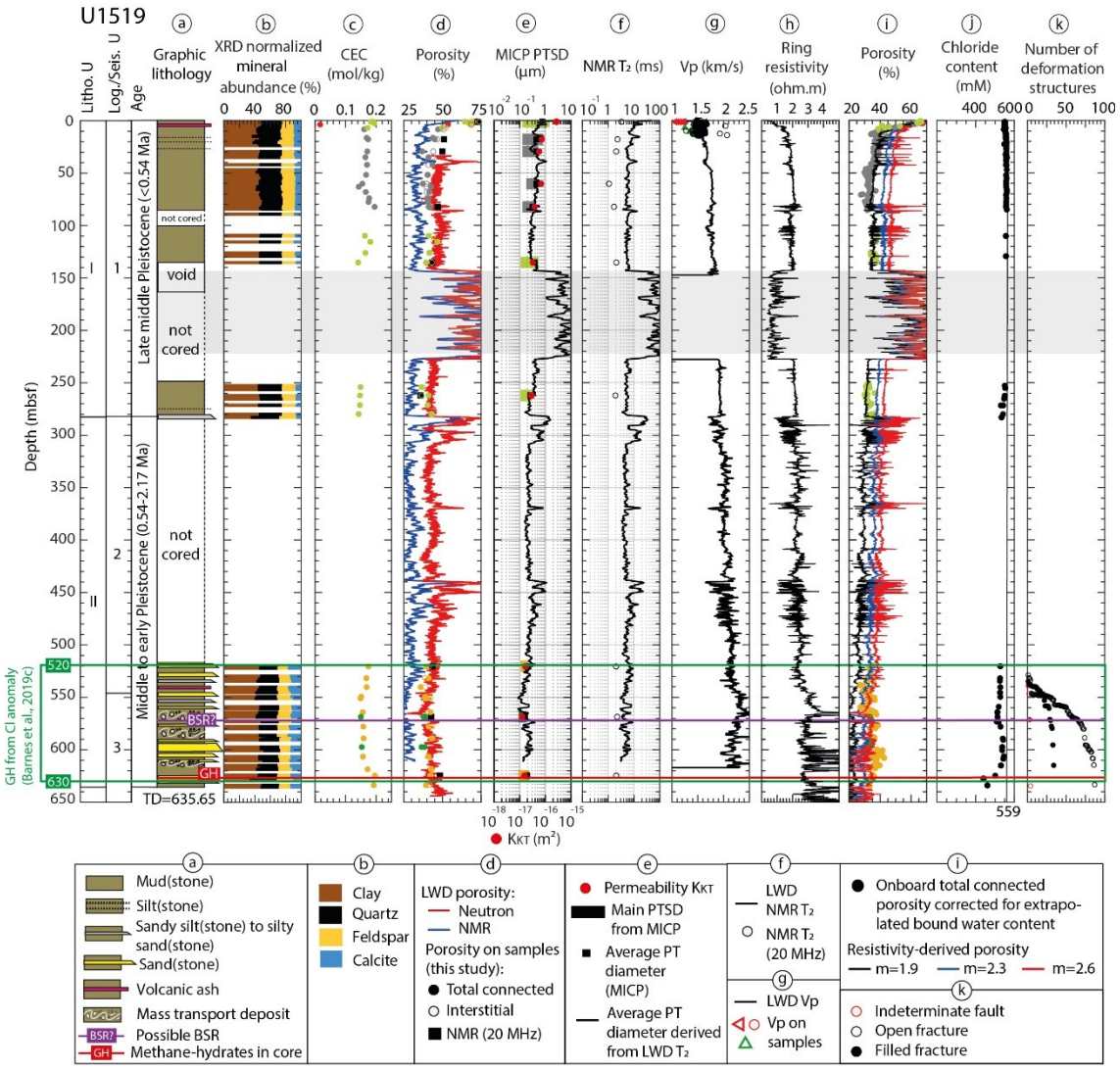

Figure 5. Summary of lithological, logging and seismic units and description (a), mineralogical (b), chemical (c and j), physical (d, e, f, g, h, i) and structural (k) properties at Site U1519. For (c), (d), (e) and (i), the colour of data points or bars indicates the lithology of the samples analysed: light green for clay(stone); green for contorted mud(stone); grey for silty clay(stone); red for ash. XRD: X-Ray diffraction; CEC: cation exchange capacity; Kkt: Katz–Thompson permeability; MICP PT(SD): mercury injection capillary pressure pore throat (size distribution) determined based on Bertrand et al. (2021); NMR: nuclear magnetic resonance; T_2: transverse relaxation time; LWD: logging-while-drilling; Vp: P-wave velocity. The green rectangle highlights a zone of gas hydrate occurrence inferred from chloride data. The grey

1066 shaded zone represents a washout interval ~143-227 mbsf identified onboard (Barnes et
1067 al., 2019c). In i), the average chloride concentration in modern seawater is 559 mM. A
1068 possible bottom-simulating-reflector (BSR) is located at 560 mbsf.
1069

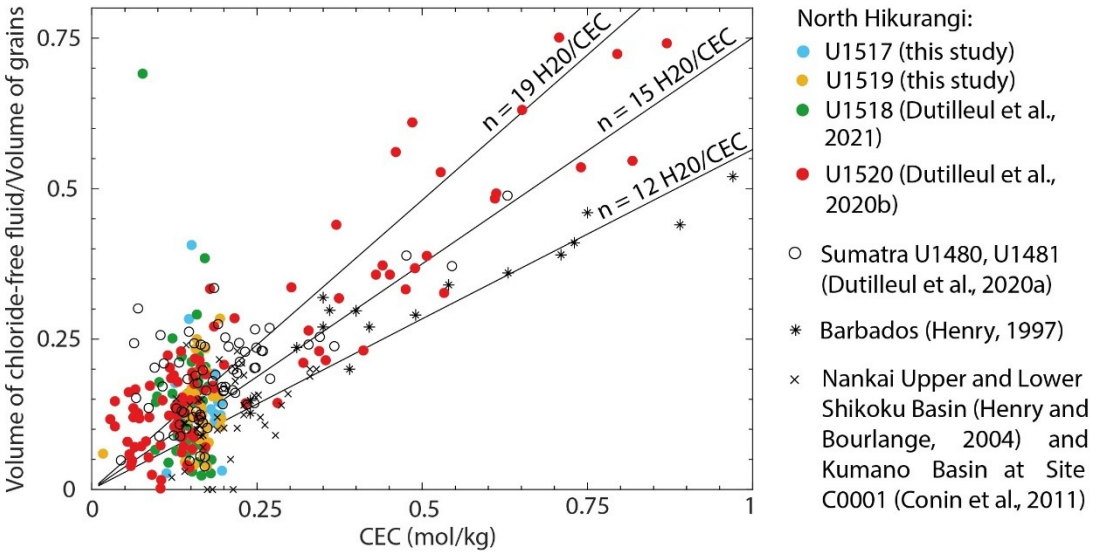

Figure 6. Bound water ratio versus Cation Exchange Capacity (CEC) at north Hikurangi margin including Site U1517 and U1519, Site U1520 (reference site across the undeformed entering sedimentary section) and U1518 (active thrust at the deformation front) and at other subduction zones from previous works.

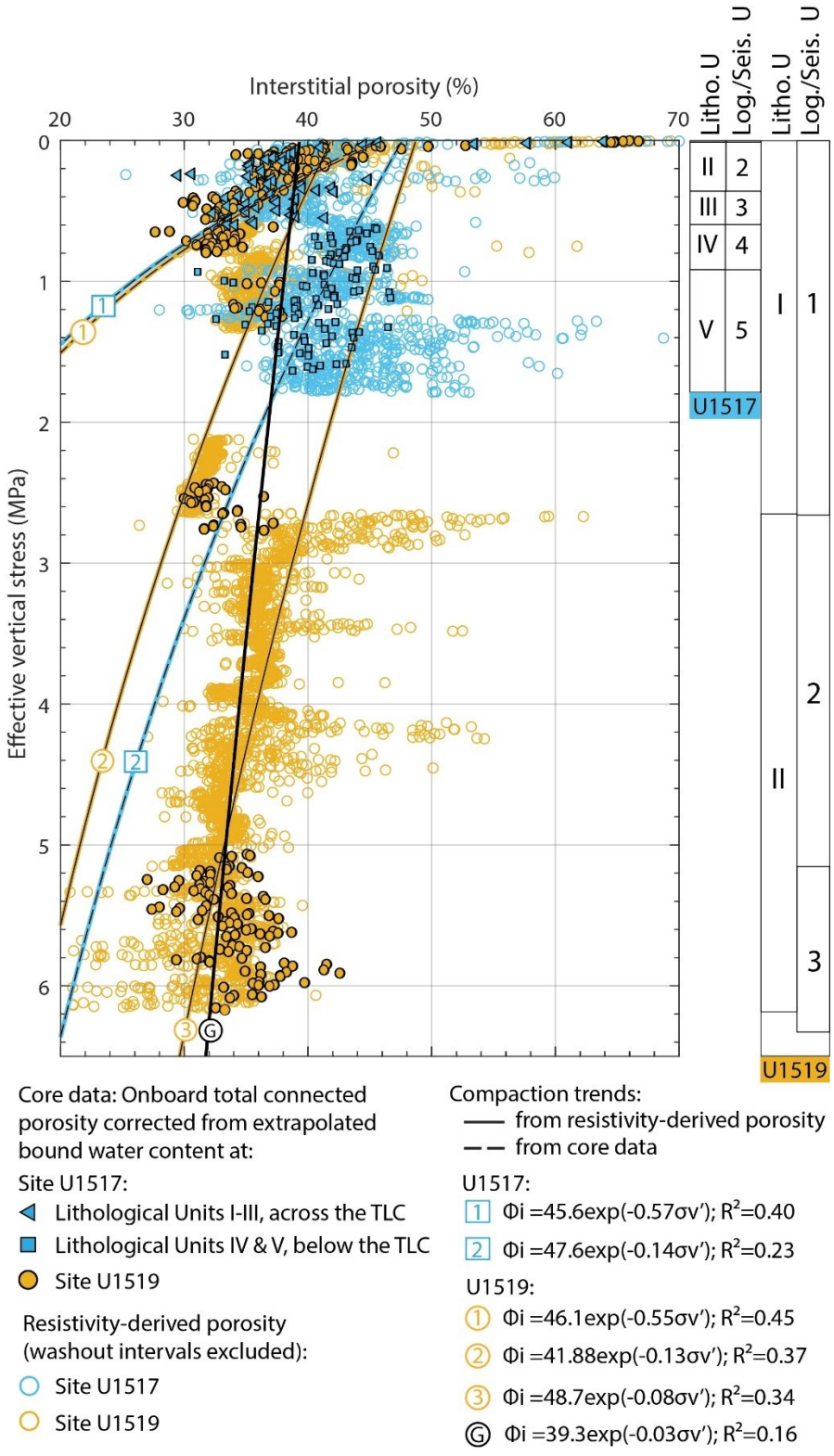

Figure 7. Summary of ring resistivity-derived porosity (open circles) calibrated to onboard interstitial porosity (i.e. total connected porosity corrected for extrapolated bound water content) (triangles, squares or circles) and compaction curves at Site U1517 (light blue) and U1519 (gold). Compaction curves determined from resistivity-

derived porosity and ‘onboard interstitial porosity’ are shown with solid lines and dashed lines respectively. The general compaction curve (trend G) at Site U1519 (excluding the washout interval ~148-227 mbsf) determined from resistivity-derived porosity is $\phi_i = 39.3 e^{-0.03\sigma'_v}$ (R^2=0.16). At Site U1519, distinct compaction trends are given (gold line numbered in open circles): trend 1) for clayey siltstones/silty claystones in lithological Unit I, trend 2) for mudstones of the same unit and trend 3) for Unit II. At Site U1517 (blue line numbered in open squares), two compaction trends were determined from onboard interstitial porosity: trend 1) is the trend for the South TLC interval and trend 2) is valid for the preslide interval.

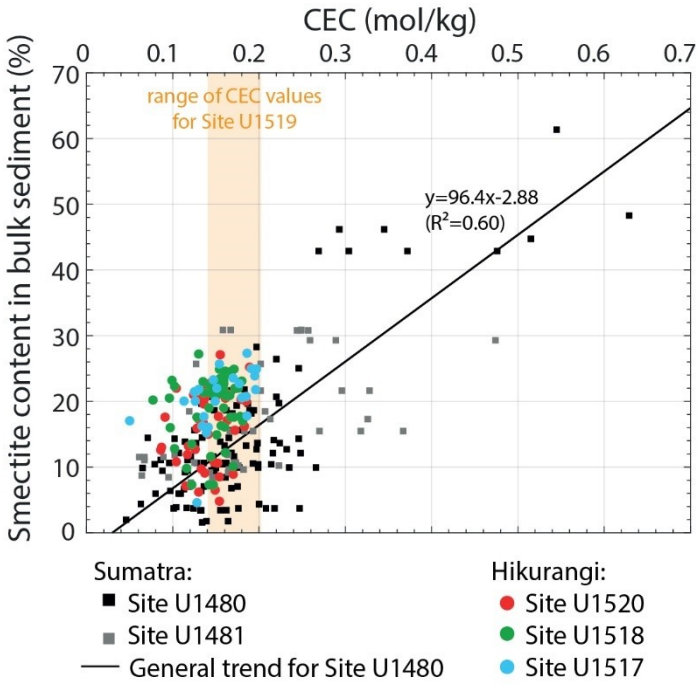

1091

1092 Figure 8. Relation between smectite content in bulk sediment determined by X-ray
1093 diffraction and cation exchange capacity (CEC) values at different IODP Sites in north
1094 Sumatra margin and north Hikurangi margin. Smectite content in bulk sediments and
1095 CEC are measured on near-by but different samples. Smectite content in bulk sediments
1096 for Sumatra Sites U1480 and U1481 are calculated from the XRD analysis of the clay
1097 fraction of Rosenberger et al. (2020) and the total clay mineral content of the nearest
1098 sample given in McNeill et al. (2017a and b). Smectite content in bulk sediments for
1099 Hikurangi Sites U1520 and U1518 are from Underwood (2021) and are from
1100 Underwood and Dugan (2021) and S. Cardona (pers. comm.) for Site U1517. CEC data
1101 for Sumatra Sites are from Dutilleul et al. (2020a). CEC data for Hikurangi Sites U1520
1102 and U1518 are from Dutilleul et al. (2020b) and (in press) respectively.

1103

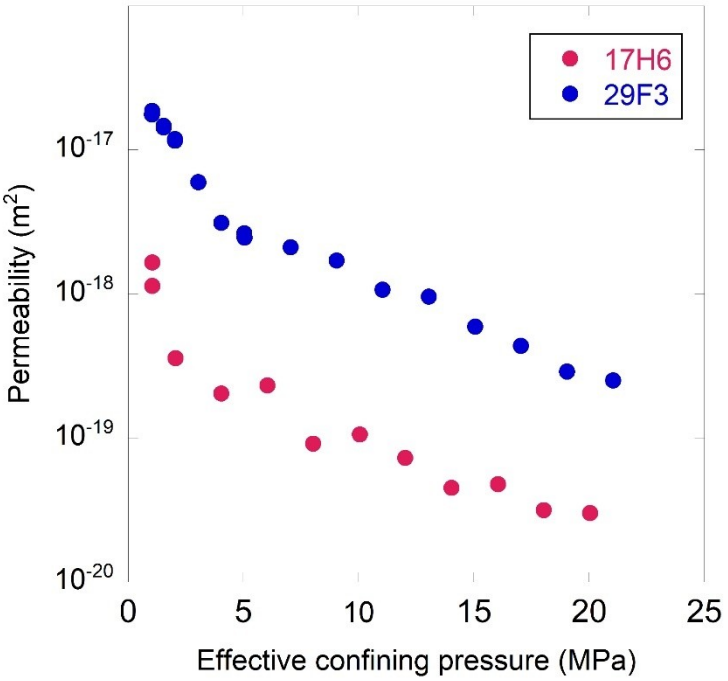

Figure 9. Permeability k as a function of effective confining pressure P_{eff} at in situ pore pressure conditions for samples 17H6 (97.43 mbsf; clayey silt) and 29F3 (157.83 mbsf; alternating sand and mud layers) from Site U1517.

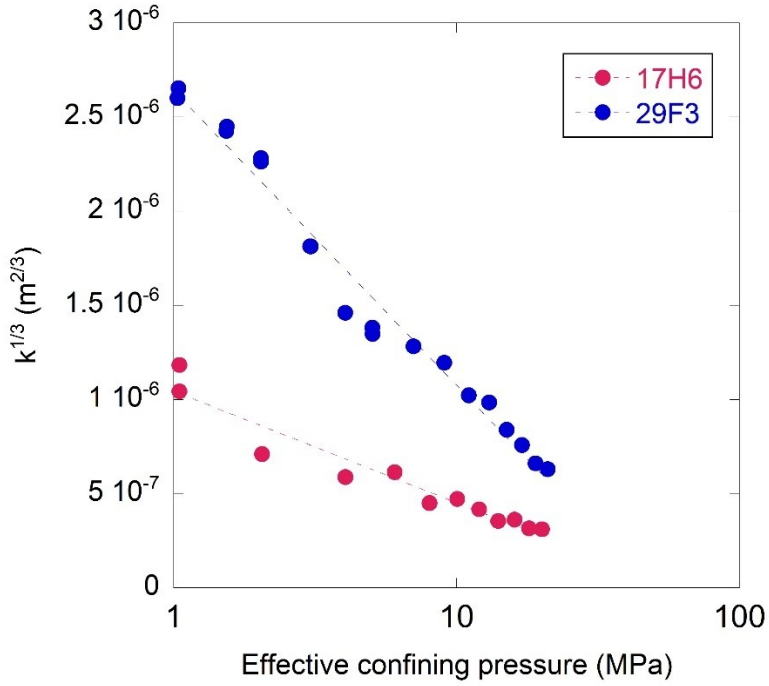

1109

1110 Figure 10. Permeability data of Figure 9 plotted as $k^{1/3}$ as a function of P_{eff} in a linear-log

1111 graph showing a linear trend consistent with the fracture closure model proposed by

1112 Walsh (1981) for samples 17H6 (97.43 mbsf; clayey silt) and 29F3 (157.83 mbsf;

1113 alternating sand and mud layers) from Site U1517.

1114

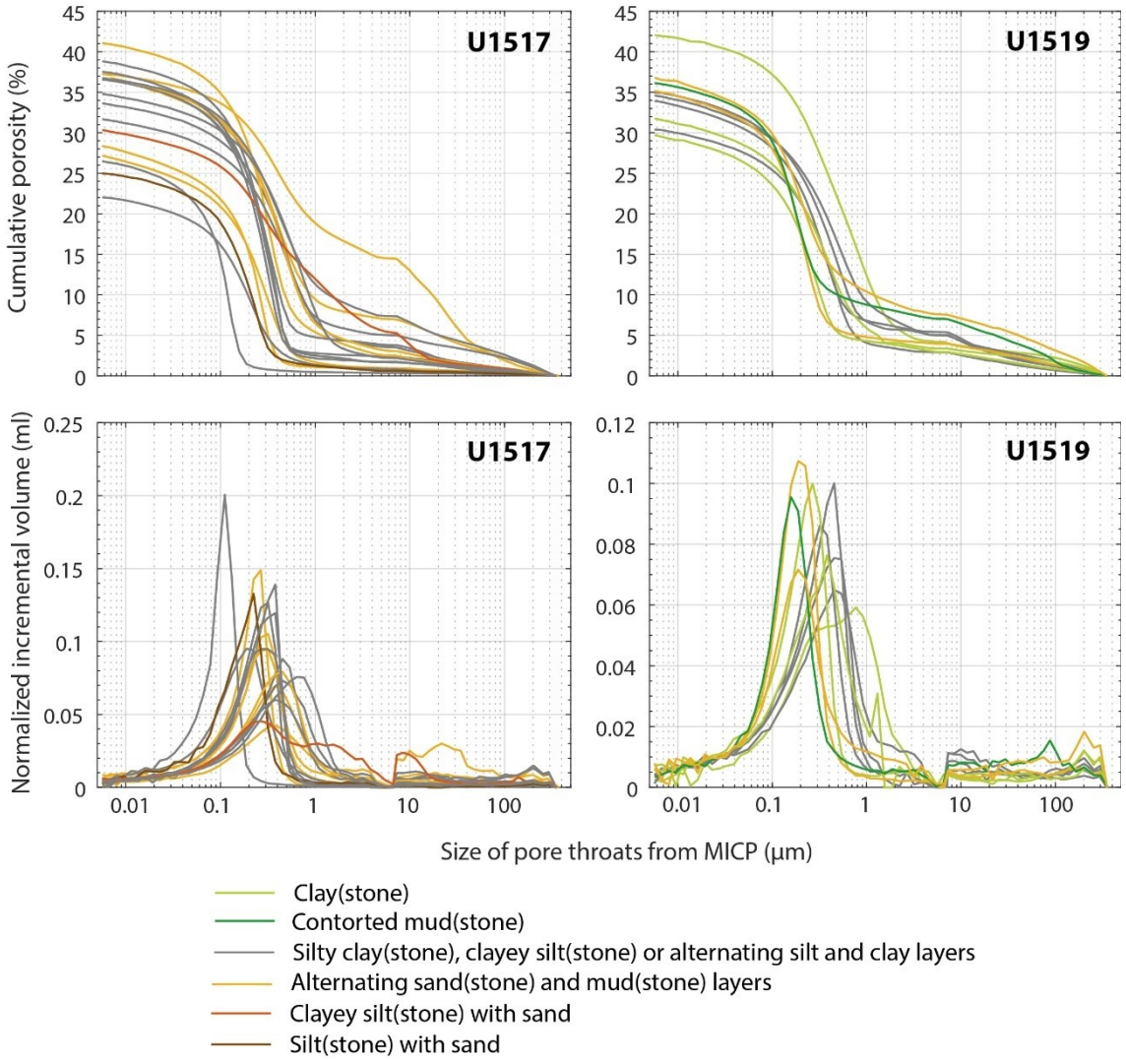

1115

1116 Figure 11. MICP pore-thoat size distribution spanning common lithologies at Site

1117 U1517 and U1519 versus cumulative porosity and normalised incremental injection

1118 volume.